Coastal Engineering 165 (2021) 103865

Contents lists available at ScienceDirect

Coastal Engineering

journal homepage: http://www.elsevier.com/locate/coastaleng

A high-performance three-dimensional lattice Boltzmann solver for water waves with free surface capturing

Guangwei Liu [a], Jinfeng Zhang [b,c], Qinghe Zhang [b,*]

[a] State Key Laboratory of Hydroscience and Engineering, Department of Hydraulic Engineering, Tsinghua University, Beijing, 100084, China
[b] State Key Laboratory of Hydraulic Engineering Simulation and Safety, Tianjin University, Tianjin, 300072, China
[c] Key Laboratory of Earthquake Engineering Simulation and Seismic Resilience of China Earthquake Administration, Tianjin University, Tianjin, 300350, China

ARTICLE INFO

Keywords:
Lattice Boltzmann method
3D collision operator
3D numerical wave simulation
High-performance computing
Wave generation and active absorption
Free surface model

ABSTRACT

The lattice Boltzmann method (LBM) is a numerical method with high parallel computational efficiency. However, currently few 3D numerical wave model based on LBM can be widely applied to water wave simulations in coastal engineering due to several problems related to numerical instability and numerical accuracy. To develop a high-performance 3D LBM solver for water wave simulations with free surface capture, a new 3D collision operator with sufficient numerical stability for wave simulation is first proposed. Then, wave generation and active wave absorption methods for the volume of fluid coupled with LBM are implemented in the solver to ensure accurate wave motion. The performances of this solver and other popular numerical wave solvers are analyzed and compared. The parameters of the numerical model are tested and determined to simulate wave transformation around structures. Through the comparison with three benchmark physical experiments, the accuracy of the presented solver proves that the present model is a promising tool for wave propagation and transformation simulation in practice. Benchmark tests and comparisons with the IHFoam and SPHysics solvers prove that the 3D LBM solver developed in this paper has a very good computational efficiency and parallel scalability. Overall, the work in this paper provides a new high-performance 3D solver for water wave simulations with free surface capturing for coastal and ocean engineering applications.

1. Introduction

At present, Navier-Stokes equations (NSE)-based numerical models that utilize the interface capturing method (ICM) are successfully applied to the study of hydrodynamic problems caused by nearshore waves. These include the Reynolds-averaged Navier-Stokes (RANS) equation with volume of fluid (VOF) method (RANS-VOF) models (Garcia et al., 2004; Higuera et al., 2013a; Lin and Liu, 1999; Liu et al., 1999), the RANS equation with the level set method (RANS-level set) models (Bihs et al., 2016; Carrica et al., 2007) and the meshless Lagrangian models (Akbari and Namin, 2013; Dalrymple and Rogers, 2006; He et al., 2020; Liu et al., 2015; Ren et al., 2014; Shao et al., 2006). All these models have shown good numerical accuracy compared with experimental results. However, with the increasing need for three-dimensional (3D) numerical simulation of waves, the computational efficiency of using a variety of NSE-ICM models to simulate 3D wave propagations is problematic, even at the laboratory scale (Table 1). For example, with the RANS-VOF model (Maza et al., 2015), it takes at least 2 days to simulate 10 s for a typical 3D application with a grid number of 20 M on 64 CPU cores. In fact, the RANS-based model has a low computational efficiency because the model needs to iteratively solve the Poisson equation and consequently requires a large computational cost and does not have good parallel scalability (Culpo, 2010). The weak compressible smoothed particle hydrodynamics (WCSPH) method uses particles of the same size in the simulation, so the computational cost of WCSPH increases geometrically as the particle size decreases. In particular, during the wave propagation process, the uneven spatial distribution of particles varies the computational cost greatly among different partitions, which leads to a considerable degeneration in the parallel scalability (Guo et al., 2018).

To develop a high-efficiency numerical wave model, we turn to the lattice Boltzmann method (LBM). This method differs from the numerical models that directly solve the NSE in that it uses a statistical approach to discretize the NSE and obtain a local and linear lattice Boltzmann equation (LBE) (Krüger et al., 2017) that results in a much higher computational efficiency without creating a bottleneck in

* Corresponding author.
E-mail address: qhzhang@tju.edu.cn (Q. Zhang).

https://doi.org/10.1016/j.coastaleng.2021.103865
Received 16 August 2020; Received in revised form 1 February 2021; Accepted 6 February 2021
Available online 9 February 2021

Table 1
Computational efficiency $\eta_{sim} = T_s/(T_{wall}N_p)$ of the NSE-ICM models for typical 3D applications, where N_G represents the number of grids or particles, T_s represents the simulation time of the wave propagation process, N_p represents the number of CPU cores used for simulation, f_{core} represents the frequency of the CPU core, and T_{wall} represents the wall clock time consumed by the simulation.

Model	N_G (M.)	T_s (s)	N_p (cores)	f_{core} (GHz)	T_{wall} (hr)	η_{sim} ($hr^{-1}core^{-1}s \times 10^{-3}$)
RANS-VOF (Maza et al., 2015)	18.6	10	16	2.6	384	1.6
	19.4	10	64	2.6	64	2.4
RANS-VOF (Maza et al., 2016)	26.5	9	256	2.6	66	0.5
RANS-level set (Aggarwal et al., 2019)	22.3	200	256	2.6	250	3.1
WCSPH (Wen et al., 2016)	2.1	15	64	2.8	96	2.4
	4.0	20	64	2.8	120	2.6

parallel scalability (Lagrava et al., 2012; Williams et al., 2009). With the rapid development of high-performance parallel computing, the LBM has been used widely in the simulation of 3D applications due to its combination of higher computational efficiency and high accuracy with parallel computing, particularly for addressing large-scale multiscale problems (Lenz et al., 2019; Morrison and Leder, 2018; Schornbaum and Rude, 2015; Sitompul and Aoki, 2019). However, the existing numerical wave models based on LBM are almost all 2D models (Badarch et al., 2020; Dinesh Kumar et al., 2019; Janssen et al., 2013; Liu et al., 2020; Ueberrueck and Janssen, 2017) and few available 3D models exist (Miliani et al., 2021). These models use LBM to solve the Navier-Stokes equations, coupled with an interface capturing method to track the motion of surface waves, and generate waves by adding forces or applying velocity at the inlet boundary. Referring to the existing simulations of solitary and periodic waves by numerical wave models based on LBM, almost all of these simulations show the problems of numerical instability and wave dissipation (Liu et al., 2019; Thorimbert et al., 2016), which demonstrates the importance of solving these problems for the establishment of a LB numerical wave model. According to previous 3D free surface applications of LBM (Fakhari et al., 2017; Kumar et al., 2019; Sato and Koshimura, 2020; Sitompul and Aoki, 2019; Ueberrueck and Janssen, 2017) based on different velocity sets, transformation matrices and relaxation parameters, nearly all 3D numerical models with free surface show significant impact on numerical stability.

Generally, at least three common velocity sets such as D3Q15, D3Q19 and D3Q27 and many different expressions for the collision operator have been used for 3D LB models. It is still unclear how to choose an effective velocity set and collision operator to form a robust and stable kernel for a 3D LB numerical wave model. Moreover, even though the problem of surface wave dissipation in 2D was solved by using a modified LB scheme through the introduction of gravity into the pressure gradient to ensure force balance (Liu et al., 2019), the applicability of the modified LB scheme to 3D wave simulation requires further investigation. To date, to the best of our knowledge, few available 3D numerical wave models ensuring the numerical stability and eliminating the dissipation of surface waves has been developed.

In addition to the problems of numerical stability and dissipation of surface waves, the approach of wave generation and absorption for 3D LB model also must be explored. Thorimbert et al. (2016) implemented wave generation in a 3D LBM-ICM coupling model by introducing a forcing term in the LBE. However, this wave generation method can only generate regular waves and requires complex calibration through numerical tests to obtain the target wave. Liu et al. (2019) implemented wave generation using the momentum source method and wave absorption by the sponge layer in a 2D LBM-ICM coupling model and achieved long-duration wave simulation without reflection. However, the use of the force method will increase the size of simulation domain, and thus will decrease the computational efficiency. Badarch et al., (2020) implemented wave generation at the inlet boundary by applying a mean velocity of shallow water waves, but they did not consider the absorption of surface waves. Generally, for the 3D LB numerical wave simulation, a complete set of wave generation and wave absorption methods is required that can generate various wave types and absorb reflected and outgoing waves.

Therefore, the aim of this paper is to present a robust, stable and high-performance 3D water wave simulation solver based on the LBM that has superior parallel scalability and computational efficiency and equivalent numerical accuracy to that of the RANS-based and meshless Lagrangian models. It is anticipated that such a solver can simulate various nearshore wave transformation processes, eliminating re-reflection waves at the open boundary of wave generation.

The paper is organized as follows. The numerical model including the LBM for NS-VOF model and the theory of wave generation and an absorption method in the 3D LBM solver is introduced in section 2. A new D3Q27 multi-relaxation-time (MRT) collision operator is described in section 3. The sensitivity analysis of spatial and temporal steps is given in section 4. Complex wave transformation around structures is simulated using the developed model, and the computational performance is evaluated in section 5. A detailed comparison of the performances of the LBM solver presented in this paper, the IHFoam solver and the SPHysics solver is conducted in section 6. Finally, conclusions are presented in section 7.

2. Numerical model

The present model uses LBM to solve the N–S equations, coupled with the VOF method to track the motion of surface waves, and generates and absorb waves by the open boundary condition.

2.1. Lattice Boltzmann method for NS-VOF model

The incompressible N–S equations are first discretized through statistical method to obtain a lattice Boltzmann equation, and then the characteristic method and trapezoidal time integral method are applied to the LBE to obtain a fully discretized LBE with second-order time and space accuracy. The discretized LBE with the *D3Qq* velocity set and the collision operator (d'Humières et al., 2002) is represented by

$$f_\alpha(\mathbf{x}+\mathbf{e}_\alpha\delta_t, t+\delta_t) - f_\alpha(\mathbf{x},t) = -\mathbf{M}^{-1}\left[\widehat{\mathbf{S}}(\mathbf{m}-\mathbf{m}^{eq})\right] \quad (1)$$

where $f_\alpha(\mathbf{x},t)$ denotes the fluid particle distribution at lattice position $\mathbf{x}$ and time t, with velocity $\mathbf{e}_\alpha$ and α ranging from 0~q - 1 in three dimensions. The particle speed is $c = \delta_x/\delta_t$; δ_x is the lattice constant; and δ_t is the time step. $\mathbf{M}$ is the transformation matrix. $\widehat{\mathbf{S}}$ is the diagonal collision matrix in moment space, which controls the numerical stability of the simulation. $\mathbf{m} = \mathbf{M}\cdot\mathbf{f}^T$ is the vector of moments; $\mathbf{f}^T \equiv [f_0, f_1, \ldots, f_{q-1}]^T$ is the vector of particle distribution functions; and $\mathbf{m}^{eq} = \mathbf{M}\cdot\mathbf{f}^{eq}$ is the vector of equilibrium moments. When the relaxation parameters are the same, the collision operator is single-relaxation-time (SRT), else it is MRT. A detailed description of the MRT collision operator used in this paper is provided in section 3.

The macro velocity and pressure are obtained from the distribution function

$$p^* = \frac{c^2}{3}\sum_\alpha f_\alpha, \quad \mathbf{u} = \sum_\alpha f_\alpha \mathbf{e}_\alpha/\rho_0 \quad (2)$$

where $\mathbf{u}$ is the vector of fluid velocity, where $p^* = p - \rho_0\mathbf{g}\cdot\mathbf{x}$ is the modified pressure (Liu et al., 2019), p is the pressure of fluid, ρ_0 is the reference density of the fluid, $\mathbf{g} = (0, -g, 0)$ is the vector of gravity acceleration and $g = 9.81\ m/s^2$. The incompressible NSE derived from the

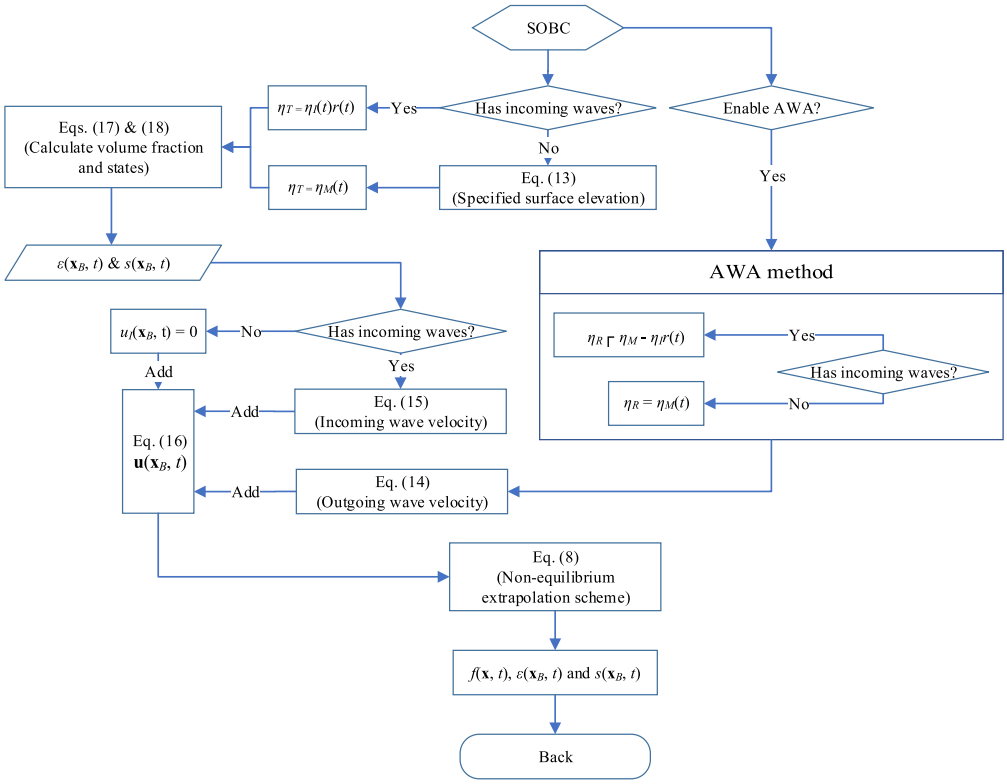

Fig. 1. Flowchart of the SOBC implemented in the present model.

modified LBE using the Maxwell iteration method (Yong et al., 2016) are written as

$$\nabla \cdot \mathbf{u} = O\left(\delta_x^2\right) \tag{3}$$

$$\frac{\partial \mathbf{u}}{\partial t} + \nabla \cdot \mathbf{u}\mathbf{u} = -\frac{\nabla p^*}{\rho_0} + \nu_{total}\nabla^2 \mathbf{u} + O\left(\delta_x^2\right) \tag{4}$$

where $\nu_{total} = \nu + \nu_t$, ν is the kinetic viscosity of water, and ν_t is the eddy viscosity related to turbulent flow.

The Smagorinsky eddy viscosity model (Krafczyk et al., 2003) is used to simulate turbulent flows, and then the LBE-large eddy simulation (LES) model is established. The eddy viscosity ν_t is calculated by the mean strain rate $\overline{\mathbf{S}}$,

$$\nu_t = (C_s\Delta)^2\left\|\overline{\mathbf{S}}\right\| \tag{5}$$

where $C_s = 0.15$ is the Smagorinsky constant, $\Delta = \delta_x$ is the filter length, and $\left\|\overline{\mathbf{S}}\right\| = \sqrt{2\overline{S}_{ij}\overline{S}_{ij}}$.

In the LBE, the mean strain rate $\overline{\mathbf{S}}$ is calculated by the non-equilibrium part of the mean second-order moment $\overline{\mathbf{\Pi}}$:

$$\overline{S}_{ij} = \frac{3\overline{\Pi}_{ij}}{-2\tau_{total}\rho_0 c^2\delta_t} \tag{6}$$

where $\overline{\Pi}_{ij} = \sum_{\alpha=0}^{q-1}\mathbf{e}_{\alpha i}\mathbf{e}_{\alpha j}f_\alpha - \rho_0 u_i u_j - p^*\delta_{ij}$ and $\tau_{total} = \frac{3\nu_{total}}{c^2\delta_t} + \frac{1}{2}$ is the relaxation time in the LBE-LES model. The relaxation time τ_{total} is expressed as

$$\tau_{total} = \frac{1}{2}\tau + \frac{1}{2}\sqrt{\tau^2 + \frac{18(C_s\Delta)^2}{\rho_0 c^4 {\delta_t}^2}|\overline{\mathbf{\Pi}}|} \tag{7}$$

where $|\overline{\mathbf{\Pi}}| = \sqrt{2\overline{\Pi}_{ij}\overline{\Pi}_{ij}}$.

The free surface is captured using the single-phase VOF method (Thuerey, 2003). This method uses a strictly bounded function to represent the volume fraction of the liquid phase. The volume fraction function is calculated by solving the convection equation.

$$\frac{\partial \varepsilon}{\partial t} + \mathbf{u}\cdot(\nabla\varepsilon) = 0 \tag{8}$$

Since the motion of air is not simulated in the single-phase model, a phase state function is defined.

$$s(\mathbf{x},t) = \begin{cases} Gas, \varepsilon(\mathbf{x},t) = 0 \\ Surface, 0 < \varepsilon(\mathbf{x},t) < 1 \\ Liquid, \varepsilon(\mathbf{x},t) = 1 \end{cases} \tag{9}$$

The wall, slip and open boundary conditions in LBM are implemented by the reconstruction of the density distribution functions streaming from the boundaries. The non-equilibrium extrapolation velocity scheme (Guo et al., 2002) is used to perform the reconstruction and is expressed as

$$f_\alpha(\mathbf{x}, t+\delta_t) = f_\alpha(\mathbf{x}+\mathbf{e}_\alpha, t+\delta_t) + f_\alpha^{eq}[p^*(\mathbf{x},t), \mathbf{u}(\mathbf{x}_B,t)] - f_\alpha^{eq}[p^*(\mathbf{x},t), \mathbf{u}(\mathbf{x},t)] \tag{10}$$

where $\mathbf{x} = \mathbf{x}_B + \mathbf{e}_\alpha$ represents the position of the target lattices and $\mathbf{x}_B$ represents the position of the boundary. A non-equilibrium extrapolation scheme is selected to reconstruct the density distribution function mainly because of its high numerical stability and parameter adaptability.

The free surface Körner (FSK) scheme (Bogner et al., 2015; Körner et al., 2005) is introduced to close the LBE-LES model at surface lattices, and is expressed as follows

$$f_\alpha(\mathbf{x}, t+\delta_t) = -f_\beta(\mathbf{x}+\mathbf{e}_\beta, t+\delta_t) + f_\alpha^{eq}\left(p_b^*, \mathbf{u}_b\right) + f_\beta^{eq}\left(p_b^*, \mathbf{u}_b\right) \tag{11}$$

where $\mathbf{x}$ represents the location of the surface lattice; f_β is the distribution function corresponding to the velocity $\mathbf{e}_\beta = -\mathbf{e}_\alpha$; p_b^* is the boundary value for the pressure at the interface and is equal to the modified pressure of the surrounding gas, which is set to $-\rho_0\mathbf{g}\cdot\mathbf{x}_b$ in our model,

where $\mathbf{x}_b$ represents the location of the interface; and $\mathbf{u}_b$ is the velocity at the interface and must be extrapolated to the boundary from the lattices.

2.2. Wave generation and absorption

The existing literature on the wave model based on the LBM includes little discussion about wave generation and absorption methods. Therefore, the details of the implementation of wave generation and absorption methods in the present model are presented in this section. The static open boundary wave generator (Higuera et al., 2013a) and active wave absorption (AWA) method (Schäffer Hemming and Klopman, 2000) are adopted for the reduction in computational costs from those of the internal wave maker and passive wave absorption method.

Here, a static open boundary condition (SOBC) (Fig. 1) is applied in the model for both wave generation and wave absorption, in which the main difference between wave generation and wave absorption is the calculation of velocity in the lattice of the open boundaries.

For wave absorption purposes, the velocity induced by the outgoing waves is obtained through the AWA method. Higuera et al. (2013a) compared several expressions of velocity perpendicular to the open boundary and suggested that the expression based on the shallow water wave theory absorbs the outgoing wave best. The mean velocity induced by the outgoing wave is given as

$$\overline{u}_R = \frac{C}{h+\eta_M(t)}\eta_R(t) \tag{12}$$

where $C = \sqrt{g[h+\eta_M(t)]}$ is the wave celerity, h is the mean water depth, $\eta_R(t)$ is the surface elevation of outgoing waves at the open boundary, and $\eta_M(t)$ is the surface elevation of one grid size away from the open boundary at time t and is given as

$$\eta_M(t) = \int_{y_{min}}^{y_{max}} \varepsilon(\mathbf{x}_B - \mathbf{n}\delta_x, t)dy - h \tag{13}$$

where y_{min} is the height of the bottom, y_{max} is the height of the top, $\mathbf{x}_B$ represents the position of the open boundary lattice, and $\mathbf{n}$ is the unit normal vector pointing out of the open boundary. When there is an incoming wave at the open boundary, the surface elevation of the outgoing wave can be approximated by $\eta_R \approx \eta_M - \eta_I r(t)$, where η_I is the surface elevation of the incoming wave; otherwise, $\eta_R = \eta_M$. The velocity induced by the outgoing wave is then obtained by the normal component:

$$\mathbf{u}_R(\mathbf{x}_B, t) = \overline{u}_R(\mathbf{x}_B, t)\mathbf{n} \tag{14}$$

For wave generation purposes, the expression of the velocity induced by the incoming wave at the open boundary is given as

$$\mathbf{u}_I(\mathbf{x}_B, t) = \varepsilon(\mathbf{x}_B, t)r(t)\mathbf{u}_T(\mathbf{x}_B, t) \tag{15}$$

where $\varepsilon(\mathbf{x}_B, t)$ is the volume fraction function at boundary lattice $\mathbf{x}_B$, $\mathbf{u}_T(\mathbf{x}_B, t)$ is the velocity corresponding to the wave theory or experimental data of the incoming wave, and $r(t)$ is the ramp coefficient, which is used to ramp the model from the static initial field and avoid the generation of standing waves near the open boundary.

Finally, the velocity exerted on the open boundary lattice is composed of two parts: the velocity induced by incoming waves and those induced by outgoing waves. The velocity in the lattices of the open boundary is then calculated as follows:

$$\mathbf{u}(\mathbf{x}_B, t) = \begin{cases} \mathbf{u}_I(\mathbf{x}_B, t) + \mathbf{u}_R(\mathbf{x}_B, t), y \le \eta_M + \dfrac{\delta_x}{2} \\ \mathbf{u}_I(\mathbf{x}_B, t), y > \eta_M + \dfrac{\delta_x}{2} \end{cases} \tag{16}$$

For a SOBC, the volume fraction functions $\varepsilon(\mathbf{x}_B, t)$ and phase states $s(\mathbf{x}_B, t)$ of the open boundary lattices are evaluated according to the specified surface elevation η_T at the open boundary. When there is an incoming wave at the open boundary, the elevation of the incoming wave is specified to the open boundary, $\eta_T = \eta_I(t)r(t)$. While there is no incoming wave at the open boundary, the elevation of one grid size away from the open boundary is specified to the open boundary, $\eta_T = \eta_M(t)$.

Following Higuera et al. (2013a), the volume fraction function at the open boundary can be evaluated according to the mass conservation $\eta_T(t) + h = \int_{y_{min}}^{y_{max}} \varepsilon(\mathbf{x}_B, t)dy$ and the nonbreaking assumption. Then, the volume fraction function in lattices of the open boundary is calculated as follows:

$$\varepsilon(\mathbf{x}_B, t) = \begin{cases} 0, y - \dfrac{\delta_x}{2} > \eta_T + h \\ \left(\dfrac{\eta_T + h - y}{\delta_x} + \dfrac{1}{2}\right), y + \dfrac{\delta_x}{2} > \eta_T + h \\ 1, y + \dfrac{\delta_x}{2} \le \eta_T + h \end{cases} \tag{17}$$

and the expression of the phase state in lattices of the open boundary is given as

$$s(\mathbf{x}_B, t) = \begin{cases} Gas, y - \dfrac{\delta_x}{2} > \eta_T + h \\ Surface, y + \dfrac{\delta_x}{2} > \eta_T + h \\ Liquid, y + \dfrac{\delta_x}{2} \le \eta_T + h \end{cases} \tag{18}$$

where y is the vertical coordinate.

Using Eq. (1) to solve the hydrodynamics of wave motions, solving Eq. (8) to capture the movement of the free surface, using the SOBC to generate and absorb waves at the open boundaries, and reconstructing the particle density distribution functions streaming from boundary lattices by Eq. (10) and Eq. (11), a 3D numerical wave model based on the LBM can be established.

2.3. Implementation of the lattice Boltzmann solver

The LB solver uses the model and methods of sections 2.1 and 2.2 for numerical simulation. The simulation procedures are as follows.

(1) Set wave simulation parameters, partition simulation domain and construct mesh;
(2) Set boundary conditions and wave gauges;
(3) Initialize particle density distributions;
(4) Time evolution
  (4.1) Collide with LES model, stream and calculate macro moments;
  (4.2) Generate and absorb waves on open boundaries;
  (4.3) Construct particle density distribution functions by boundary schemes;
  (4.4) Perform single-phase free surface VOF model;
  (4.5) Output flow fields, gauge pressures and water elevations;
  (4.6) Repeat steps 4.1–4.5 until the final solutions are obtained;
(5) Output computational time and computational performance results;

A detailed description of the implementation of step 4.4 can be found in Thuerey (2003). The structure of the array data layout, code vectorization, and MPI/OpenMP hybrid are adopted in this solver to improve the computational performance. The MPI acceleration will lead to a communication delay in steps 4.1 and 4.4, this time cost is taken into account in the analysis of computational performance results obtained in step 5.

Table 2
Five existing collision operators with the relaxation parameters related to shear viscosity set to $1/\tau$.

Collision operator	Relaxation parameters
D3Q19-SRT (He and Luo, 1997a)	$s_\alpha = 1/\tau$
D3Q19-MRT-Humières (d'Humières et al., 2002)	$s_1 = 1.19$, $s_2 = s_{10} = 1.4$, $s_4 = 1.2$ and $s_{16} = 1.98$
D3Q19-MRT-Janssen (Janssen and Krafczyk, 2010)	$s_1 = 0.3$ and $s_2 = s_4 = s_{10} = s_{16} = 1.0$
D3Q27-SRT (He and Luo, 1997a)	$s_\alpha = 1/\tau$
D3Q27-MRT-Suga (Suga et al., 2015)	$s_4 = 1.54$, $s_{10} = 1.5$, $s_{13} = 1.83$, $s_{16} = 1.4$, $s_{17} = 1.61$, $s_{18} = s_{20} = 1.98$ and $s_{23} = s_{26} = 1.74$

3. A new D3Q27 MRT collision operator

3.1. Derivation of the new collision operator

The numerical stability of a LB model is mainly determined by the collision operator (Luo et al., 2011). Unfortunately, the five commonly-used collision operators (Table 2) all encountered numerical instability when applied to the wave model built in section 2, and most finally diverge. Therefore, to establish an applicable 3D LB numerical wave model, a more stable collision operator is needed.

The first step for proposing a collision operator is to select an appropriate velocity set as the basis of the operator. Based on the conclusions drawn from the pipeline turbulence investigations carried out by direct LBM-based numerical simulations (Kang and Hassan, 2013; Peng et al., 2018; Suga et al., 2015), the D3Q27 collision operator shows better performance than the D3Q19 collision operator in 3D turbulence simulation, and it is speculated that the isotropy of the D3Q27 velocity set is better (Peng et al., 2018). Therefore, we choose to construct the collision operator based on the D3Q27 velocity set for the LB wave model.

Table 3
Wave, flume and model parameters.

Parameter	Value	Parameter	Value
Wave height (H)	0.24 m	Water depth (d)	0.8 m
Wave celerity (C)	3.19 m/s	Flume height	1.16 m
Flume width (W)	2.65 m	Flume length	20.0 m
Lattice constant (δ_x)	0.03 m	Time step (δ_t)	6.01×10^{-4} s
Ma_{LB}	0.064	Relaxation time (τ)	0.500002
Simulation time	12.0 s		

After summarizing the simulation results of the 3D wave model built in section 2 based on the five collision operators, we find that the D3Q19-MRT collision operator proposed by Janssen and Krafczyk (2010) maintains the longest stable time. We compared their collision operator with the other operators and find two characteristics that may be the key origins of the better stability of the D3Q19-MRT collision operator: (1) The equilibrium of the third- and higher-order velocity moments is zero; and (2) the relaxation parameter independent of bulk viscosity and shear viscosity is one. Therefore, we construct a new MRT collision operator based on the D3Q27 velocity set based on these two characteristics.

To obtain the MRT collision operator satisfying the above characteristics, we carry out the elimination operation to the orthogonalized D3Q27 transformation matrix proposed by Suga et al. (2015) until it meets the characteristic 1. Finally, the transformation matrix of the new collision operator is given by

$$\mathbf{M} = \begin{bmatrix}
1 & 1 & 1 & 1 & 1 & 1 & 1 & 1 & 1 & 1 & 1 & 1 & 1 & 1 & 1 & 1 & 1 & 1 & 1 & 1 & 1 & 1 & 1 & 1 & 1 & 1 & 1 \\
0 & 1 & -1 & 0 & 0 & 0 & 0 & 1 & -1 & 1 & -1 & 1 & -1 & 1 & -1 & 0 & 0 & 0 & 0 & 1 & -1 & 1 & -1 & 1 & -1 & -1 & 1 \\
0 & 0 & 0 & 1 & -1 & 0 & 0 & 1 & 1 & -1 & -1 & 0 & 0 & 0 & 0 & 1 & -1 & 1 & -1 & 1 & -1 & 1 & -1 & -1 & 1 & 1 & -1 \\
0 & 0 & 0 & 0 & 0 & 1 & -1 & 0 & 0 & 0 & 0 & 1 & 1 & -1 & -1 & 1 & 1 & -1 & -1 & 1 & -1 & -1 & 1 & 1 & -1 & 1 & -1 \\
-1 & 0 & 0 & 0 & 0 & 0 & 0 & 1 & 1 & 1 & 1 & 1 & 1 & 1 & 1 & 1 & 1 & 1 & 1 & 2 & 2 & 2 & 2 & 2 & 2 & 2 & 2 \\
0 & 2 & 2 & -1 & -1 & -1 & -1 & 1 & 1 & 1 & 1 & 1 & 1 & 1 & 1 & -2 & -2 & -2 & -2 & 0 & 0 & 0 & 0 & 0 & 0 & 0 & 0 \\
0 & 0 & 0 & 1 & 1 & -1 & -1 & 1 & 1 & 1 & 1 & -1 & -1 & -1 & -1 & 0 & 0 & 0 & 0 & 0 & 0 & 0 & 0 & 0 & 0 & 0 & 0 \\
0 & 0 & 0 & 0 & 0 & 0 & 0 & 1 & -1 & -1 & 1 & 0 & 0 & 0 & 0 & 0 & 0 & 0 & 0 & 1 & 1 & 1 & 1 & -1 & -1 & -1 & -1 \\
0 & 0 & 0 & 0 & 0 & 0 & 0 & 0 & 0 & 0 & 0 & 0 & 0 & 0 & 0 & 1 & -1 & -1 & 1 & 1 & 1 & -1 & -1 & -1 & -1 & 1 & 1 \\
0 & 0 & 0 & 0 & 0 & 0 & 0 & 0 & 0 & 0 & 0 & 1 & -1 & -1 & 1 & 0 & 0 & 0 & 0 & 1 & 1 & -1 & -1 & 1 & 1 & -1 & -1 \\
0 & -2 & 2 & 0 & 0 & 0 & 0 & 1 & -1 & 1 & -1 & 1 & -1 & 1 & -1 & 0 & 0 & 0 & 0 & 4 & -4 & 4 & -4 & 4 & -4 & -4 & 4 \\
0 & 0 & 0 & -2 & 2 & 0 & 0 & 1 & 1 & -1 & -1 & 0 & 0 & 0 & 0 & 1 & -1 & 1 & -1 & 4 & -4 & 4 & -4 & -4 & 4 & 4 & -4 \\
0 & 0 & 0 & 0 & 0 & -2 & 2 & 0 & 0 & 0 & 0 & 1 & 1 & -1 & -1 & 1 & 1 & -1 & -1 & 4 & -4 & -4 & 4 & 4 & -4 & 4 & -4 \\
0 & 1 & -1 & 0 & 0 & 0 & 0 & -1 & 1 & -1 & 1 & -1 & 1 & -1 & 1 & 0 & 0 & 0 & 0 & 0 & 0 & 0 & 0 & 0 & 0 & 0 & 0 \\
0 & 0 & 0 & 1 & -1 & 0 & 0 & -1 & -1 & 1 & 1 & 0 & 0 & 0 & 0 & -1 & 1 & -1 & 1 & 0 & 0 & 0 & 0 & 0 & 0 & 0 & 0 \\
0 & 0 & 0 & 0 & 0 & 1 & -1 & 0 & 0 & 0 & 0 & -1 & -1 & 1 & 1 & -1 & -1 & 1 & 1 & 0 & 0 & 0 & 0 & 0 & 0 & 0 & 0 \\
1 & -1 & -1 & -1 & -1 & -1 & -1 & 0 & 0 & 0 & 0 & 0 & 0 & 0 & 0 & 0 & 0 & 0 & 0 & 4 & 4 & 4 & 4 & 4 & 4 & 4 & 4 \\
-3 & 4 & 4 & 4 & 4 & 4 & 4 & -4 & -4 & -4 & -4 & -4 & -4 & -4 & -4 & -4 & -4 & -4 & -4 & 0 & 0 & 0 & 0 & 0 & 0 & 0 & 0 \\
0 & -2 & -2 & 1 & 1 & 1 & 1 & 2 & 2 & 2 & 2 & 2 & 2 & 2 & 2 & -4 & -4 & -4 & -4 & 0 & 0 & 0 & 0 & 0 & 0 & 0 & 0 \\
0 & 0 & 0 & -1 & -1 & 1 & 1 & 2 & 2 & 2 & 2 & -2 & -2 & -2 & -2 & 0 & 0 & 0 & 0 & 0 & 0 & 0 & 0 & 0 & 0 & 0 & 0 \\
0 & 0 & 0 & 0 & 0 & 0 & 0 & -1 & 1 & 1 & -1 & 0 & 0 & 0 & 0 & 0 & 0 & 0 & 0 & 2 & 2 & 2 & 2 & -2 & -2 & -2 & -2 \\
0 & 0 & 0 & 0 & 0 & 0 & 0 & 0 & 0 & 0 & 0 & 0 & 0 & 0 & 0 & -1 & 1 & 1 & -1 & 2 & 2 & -2 & -2 & -2 & -2 & 2 & 2 \\
0 & 0 & 0 & 0 & 0 & 0 & 0 & 0 & 0 & 0 & 0 & -1 & 1 & 1 & -1 & 0 & 0 & 0 & 0 & 2 & 2 & -2 & -2 & 2 & 2 & -2 & -2 \\
0 & 0 & 0 & 0 & 0 & 0 & 0 & 1 & -1 & 1 & -1 & -1 & 1 & -1 & 1 & 0 & 0 & 0 & 0 & 0 & 0 & 0 & 0 & 0 & 0 & 0 & 0 \\
0 & 0 & 0 & 0 & 0 & 0 & 0 & -1 & -1 & 1 & 1 & 0 & 0 & 0 & 0 & 1 & -1 & 1 & -1 & 0 & 0 & 0 & 0 & 0 & 0 & 0 & 0 \\
0 & 0 & 0 & 0 & 0 & 0 & 0 & 0 & 0 & 0 & 0 & 1 & 1 & -1 & -1 & -1 & -1 & 1 & 1 & 0 & 0 & 0 & 0 & 0 & 0 & 0 & 0 \\
0 & 0 & 0 & 0 & 0 & 0 & 0 & 0 & 0 & 0 & 0 & 0 & 0 & 0 & 0 & 0 & 0 & 0 & 0 & 1 & -1 & -1 & 1 & -1 & 1 & -1 & 1
\end{bmatrix} \tag{19}$$

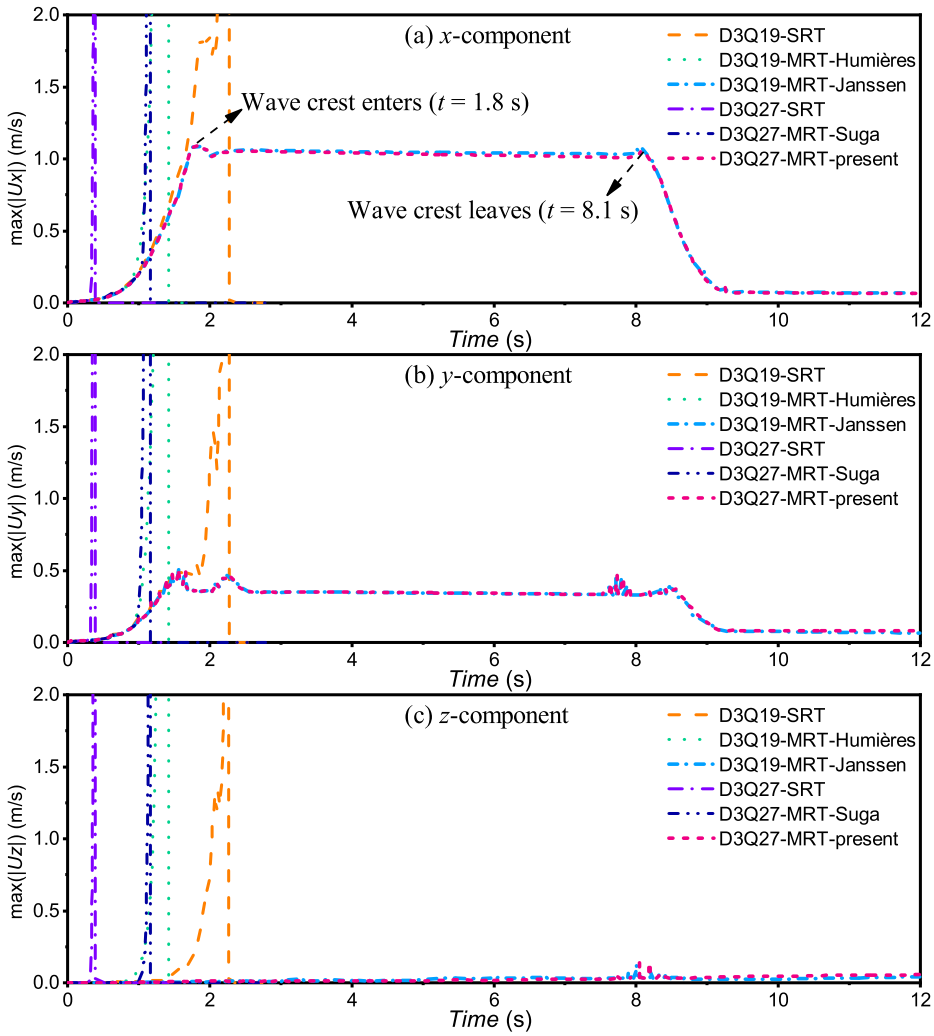

Fig. 2. Evolution of the maximum of three velocity components in the middle region for the solitary wave propagation using the five collision operators and the present collision operator.

The fluid particle velocity $\mathbf{e}_\alpha$ is given by

$$\mathbf{e}_\alpha = c\begin{bmatrix} 0 & 1 & -1 & 0 & 0 & 0 & 0 & 1 & -1 & 1 & -1 & 1 & -1 & 1 & -1 & 0 & 0 & 0 & 0 & 1 & -1 & 1 & -1 & 1 & -1 & -1 & 1 \\ 0 & 0 & 0 & 1 & -1 & 0 & 0 & 1 & 1 & -1 & -1 & 0 & 0 & 0 & 0 & 1 & -1 & 1 & -1 & 1 & -1 & 1 & -1 & -1 & 1 & 1 & -1 \\ 0 & 0 & 0 & 0 & 0 & 1 & -1 & 0 & 0 & 0 & 0 & 1 & 1 & -1 & -1 & 1 & 1 & -1 & -1 & 1 & -1 & -1 & 1 & 1 & -1 & 1 & -1 \end{bmatrix}^T \tag{20}$$

The diagonal collision matrix is given by

$$\widehat{\mathbf{S}} \equiv diag\left(1,1,1,1,s_e,s_p,s_p,s_\nu,s_\nu,s_\nu,s_q,s_q,s_q,s_{q\varepsilon},s_{q\varepsilon},s_{q\varepsilon},s_\varepsilon,s_{\varepsilon 3},s_{\pi xx},s_{\pi xx},s_\pi,s_\pi,s_\pi,s_m,s_m,s_m\right) \tag{21}$$

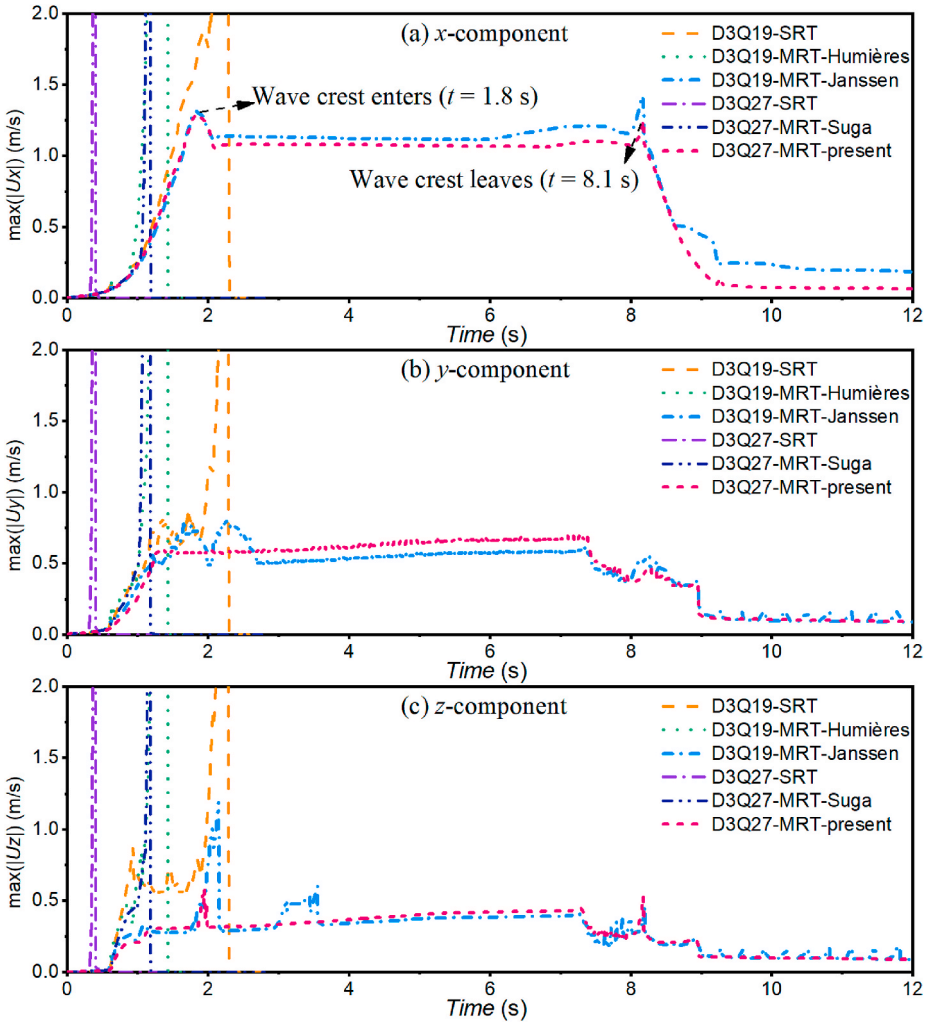

Fig. 3. Evolution of the maximum of three velocity components in the near wall region for the solitary wave propagation using the five collision operators and the present collision operator.

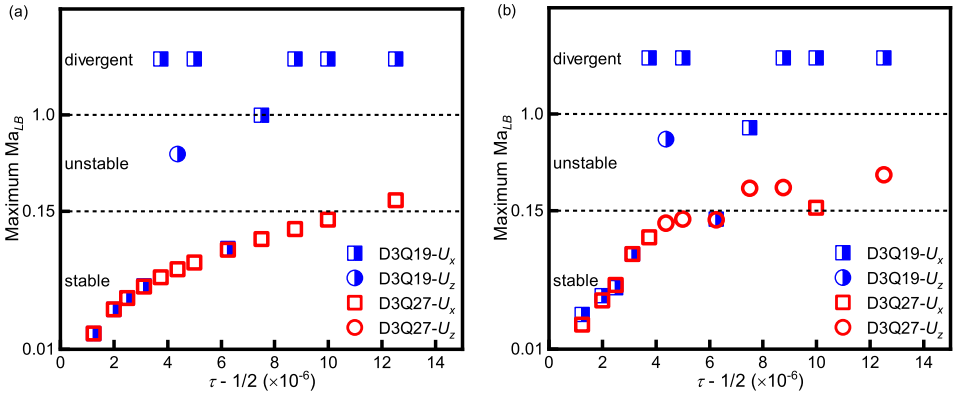

Fig. 4. Maximum local Ma_{LB} for propagation of solitary wave in the (a) middle region, (b) near-wall region, using different relaxation times. D3Q19 represents results obtained using the D3Q19-MRT-Janssen collision operator and D3Q27 represents the results obtained using the present collision operator. The stable state corresponds to the maximum Ma_{LB} less than 0.15, the unstable state corresponds to the maximum Ma_{LB} greater than 0.15 and less than 1.0, and the divergent state corresponds to divergence in the simulation. U_x means that the maximum velocity is the x component, and U_z means that the maximum velocity is the z component.

Table 4
List of numerical tests carried out for the sensitivity analysis.

No.	H (m)	h (m)	δ_x (cm)	H/δ_x	L (m)	Ma_{LB}	$\tau - 0.5$ ($\times 10^{-6}$)
(a) Determination of the grid size in the 3D model							
*A*1	0.16	0.8	4.0	4	50.0	0.064	1.6
*A*2	0.16	0.8	2.0	8	50.0	0.064	3.1
*A*3	0.16	0.8	1.0	16	50.0	0.064	6.3
*A*4	0.16	0.8	0.7	24	50.0	0.064	9.4
*A*5	0.16	0.8	0.5	32	50.0	0.064	12.5
(b) Determination of the time step in the 3D model							
*B*1	0.16	0.8	1.0	16	50.0	0.128	12.5
*B*2	0.16	0.8	1.0	16	50.0	0.096	9.4
*B*3	0.16	0.8	1.0	16	50.0	0.064	6.3
*B*4	0.16	0.8	1.0	16	50.0	0.032	3.1
*B*5	0.16	0.8	1.0	16	50.0	0.016	1.6

According to Luo et al. (2011) and Safi (2016), setting s_e to small values will improve stability, and therefore, the relaxation parameters in $\widehat{\mathbf{S}}$ are chosen as $s_e = 0.3$, $s_\alpha = 1.0$, and $s_\nu = s_p = \frac{1}{\tau}$, and the relaxation time, $\tau = 3\frac{\delta_t}{\delta_x^2}\nu + 1/2$, is coupled with the kinetic viscosity, ν.

The vector of the equilibrium moments is given by

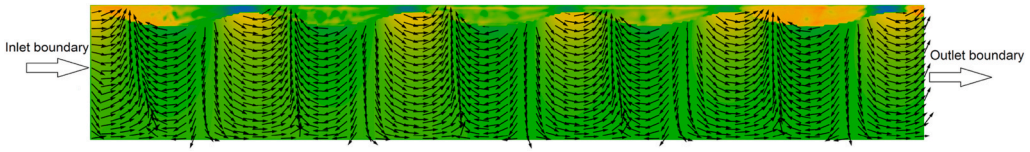

Fig. 5. Sketch of the numerical model.

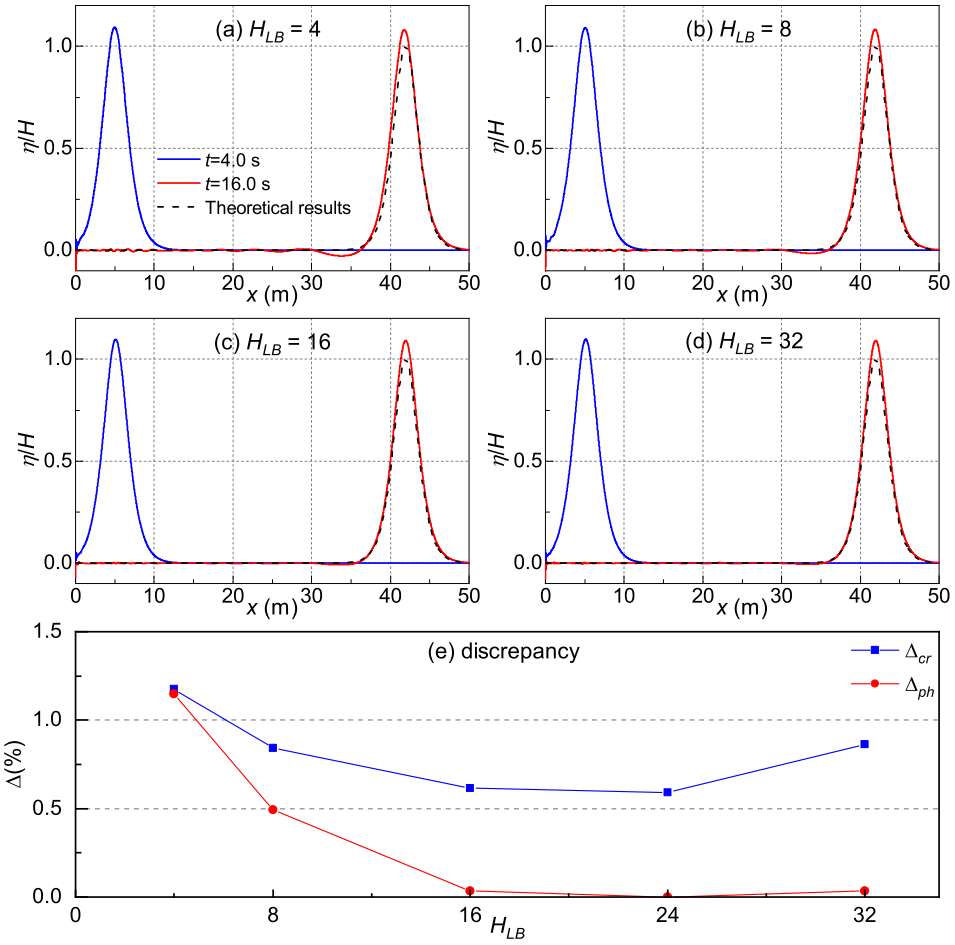

Fig. 6. Numerical results of the grid convergence study. In (a)~(d), the blue solid line shows the simulated relative surface elevation at $t = 4.0$ s, the red solid line shows the simulated relative surface elevation at $t = 16.0$ s, and the black dashed line shows the theoretical results at $t = 16.0$ s. In (e), the blue squares with blue solid lines show the discrepancy in the wave crests in the simulations, and the red circles with red solid lines show the discrepancy in the wave phases in the simulations. (For interpretation of the references to colour in this figure legend, the reader is referred to the Web version of this article.)

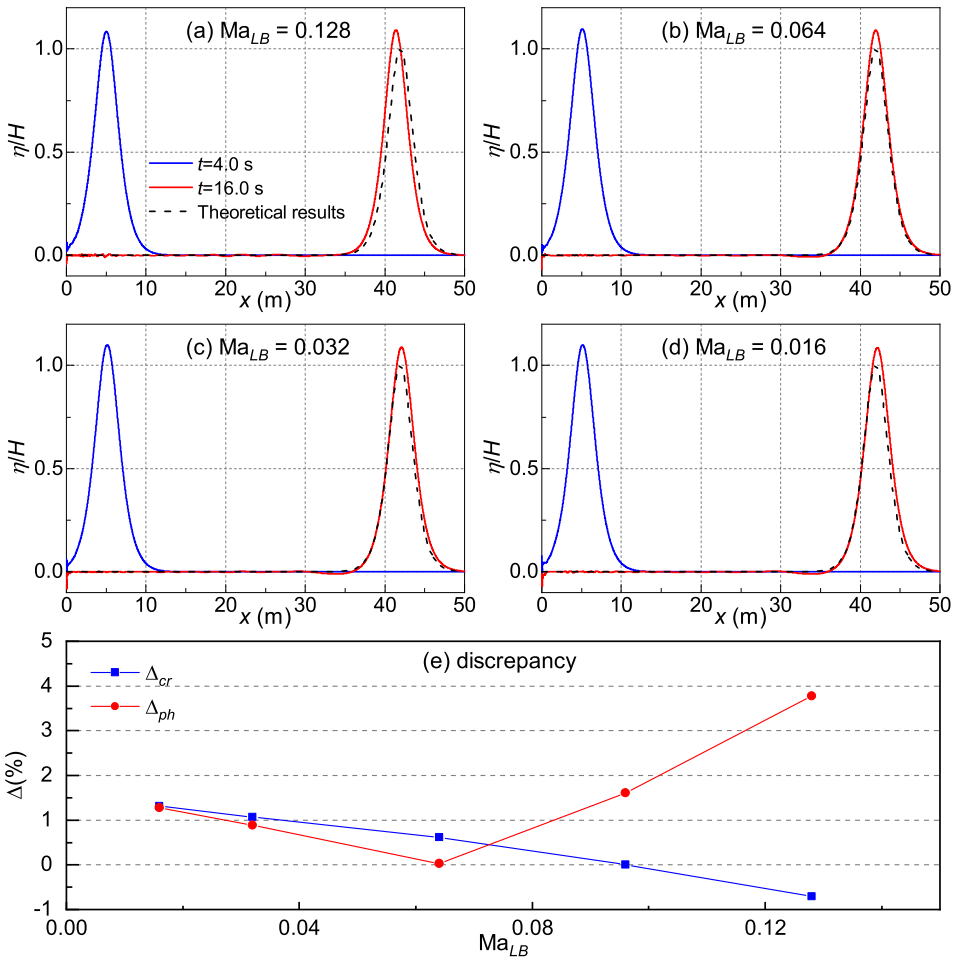

Fig. 7. Numerical results of the time step convergence study. In (a)~(d), the blue solid line shows the simulated relative surface elevation at $t = 4.0$ s, the red solid line shows the simulated relative surface elevation at $t = 16.0$ s, and the black dashed line shows the theoretical results at $t = 16.0$ s. In (e), the blue squares with blue solid lines show the discrepancy in the wave crests in the simulations, and the red circles with red solid lines show the discrepancy in the wave phases in the simulations. (For interpretation of the references to colour in this figure legend, the reader is referred to the Web version of this article.)

$$\mathbf{m}^{eq} = \left[3p^*, u_x, u_y, u_z, u_x^2+u_y^2+u_z^2, 2u_x^2-u_y^2-u_z^2, u_y^2-u_z^2, u_xu_y, u_yu_z, u_xu_z, 0,0,0,0,0,0,0,0,0,0,0,0,0,0,0,0,0\right]^T \quad (22)$$

3.2. Comparison of collision operators

Next, a solitary wave propagation in a 3D flat bottom flume is presented to show the advantages of the new collision operator with respect to numerical stability compared with the five commonly-used operators. The input solitary wave parameters, flume and model parameters are shown in Table 3. The LB Mach number (Ma$_{LB}$) in this paper is defined as the ratio of wave celerity (C_{LB}) in the LB unit to sound speed c_s; it represents the compressibility and numerical stability in the standard LBE scheme and is similar to the Courant-Friederichs-Lewy (CFL) criterion (Luo et al., 2011). The maximum velocity of the water is regarded as a relevant factor for numerical stability. The bursts or oscillations of the velocity with high frequency indicate that the numerical stability of the collision operator is poor. Local flow oscillation commonly occurs near the wall boundary, particularly at the junction of the free surface and the wall boundary. Therefore, the maximum velocity is counted in two regions of the flume, namely the middle region for which the Z coordinate is [0.25W, 0.75W] and the near-wall region for which the Z coordinate is [0, 0.24W].

In Fig. 2 and Fig. 3 we show the results of the stability test. Clearly, the D3Q19-MRT-Humières, D3Q27-SRT and D3Q27-MRT-Suga operators show the worst performance in this test. The D3Q19-SRT operator is more stable than the D3Q19-MRT-Humières, D3Q27-SRT and D3Q27-MRT-Suga operators. The D3Q19-MRT-Janssen and D3Q27-MRT present are the most stable operators, and there is no observable difference between these two collision operartors in terms of stability at the middle region. However, in the near-wall region, the stability of the D3Q19-MRT-Janssen operator deteriorates considerably, a few significant bursts occurs at the time of wave crest entering and leaving the flume, and the maximum y and z component velocity show high frequency oscillations after the wave crest leaves the flume. Compared with the middle region, the maximum z component velocity of both the D3Q19-MRT-Janssen and D3Q27-MRT-present operators in the near-wall region increases obviously. This is because the errors introduced by the reconstruction schemes for the free surface and the wall boundaries significantly increase the z component velocity. Overall, the D3Q27-MRT-present operator is more stable than the other five collision operators.

For LBM, a larger local Ma$_{LB}$ (the ratio of velocity in lattice unit to the sound speed) leads to higher computational efficiency, but lower numerical stability and accuracy. In standard LB scheme, the maximum of the local Ma$_{LB}$ cannot be larger than 0.15 to maintain the stability of the simulation (He and Luo, 1997a). Therefore, a collision operator that can maintain numerical stability and accuracy at larger local Ma$_{LB}$ is

Table 5
Detailed lists for numerical simulations of wave transformations.

Sec.	H (m)	h (m)	λ (m)	δ_x (cm)	L (m)	Ma_{LB}	$\tau - 0.5$ ($\times 10^{-6}$)	t_{end} (s)	N_g (M)	N_p (cores)	T_s (hr)	η_{sim} ($\times 10^{-3}$ hr^{-1}core^{-1}s)
4.1	0.060	0.250	3.08	0.38	20.6	0.064	33.2	24.0	77.2	120	14.3	14.0
4.2	0.068	0.205		0.28	7.5	0.064	42.0	5.0	26.3	60	5.5	15.2
4.3	0.064	0.320		1.00	25.0	0.064	10.0	15.0	174.2	360	3.9	10.7

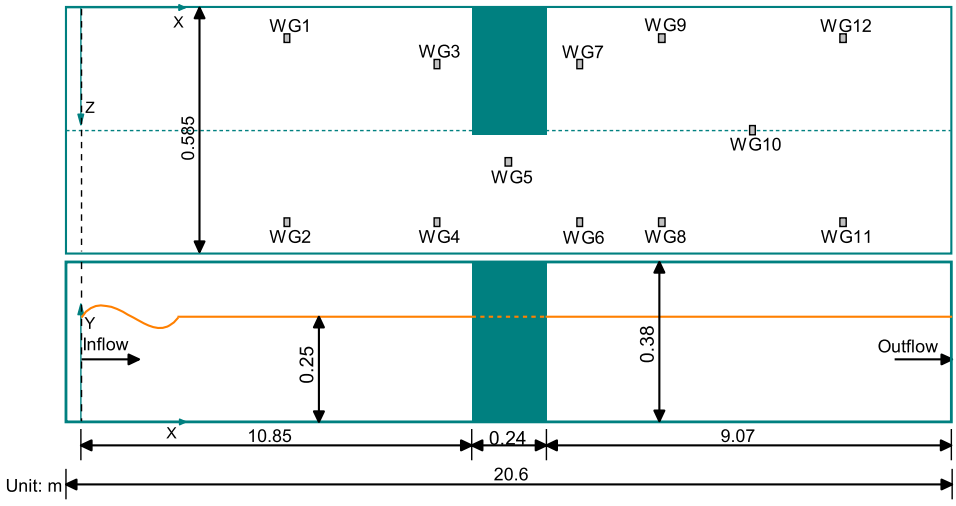

Fig. 8. Sketch of numerical experimental setup of wave transformation on a vertical structure. Gray rectangles represent the wave gauge positions.

Table 6
Wave gauge positions.

No.	X (m)	Z (m)	No.	X (m)	Z (m)
1	9.75	0.100	2	9.75	0.485
3	10.75	0.200	4	10.75	0.485
5	10.95	0.395	6	11.19	0.485
7	11.19	0.200	8	11.49	0.485
9	11.49	0.100	10	11.89	0.300
11	12.29	0.485	12	12.29	0.100

considered to show outstanding performance. Hence, the comparison between D3Q19-MRT-Janssen and D3Q27-MRT-present focuses on their stability at different Ma_{LB}. In the following, a series of solitary wave propagation cases with the same spatial step and different time steps are simulated, where smaller maximum local Ma_{LB} and the relaxation time correspond to a smaller time step. The simulation results shown in Fig. 4 demonstrate that D3Q19-MRT diverges when the relaxation time is larger than 0.500004, corresponds to Ma_{LB} larger than 0.04, while D3Q27-MRT is still broadly stable (Fig. 4(a)) for Ma_{LB} up to 0.14. In the near-wall region (Fig. 4(b)), when the relaxation time is larger than 0.500004, the maximum local Ma_{LB} is controlled by the z-component of the velocity, which is completely different from the actual physical laws that the velocity in the z direction should be much smaller than that in the x direction. This indicates the low accuracy of the results in the near-wall region, indicating the need for a further study of the numerical error in the junction of the free surface and the wall boundary. Despite its relatively low accuracy in the near-wall region, the present D3Q27-MRT collision operator show much better stability than D3Q19-MRT in wave simulations.

The results show that the new D3Q27 MRT collision operator is more stable than the five commonly used collision operators. In the following sections, the 3D numerical wave model based on the new collision operator will be used for numerical wave simulation.

4. Sensitivity analysis of spatial and temporal step

In this section, the selection of the proper grid size and time step for the presented numerical model is conducted. The details of the numerical tests carried out for the validation are listed in Table 4. The length (L) and width of the wave tank are fixed to 50.0 m and $2\delta_x$, respectively, in this study. Solitary wave simulation is chosen to conduct a sensitivity analysis. The grid size is tested through simulations in different grid sizes of $\delta_x = 4.0$ cm, 2.0 cm, 1.0 cm, 0.7 cm and 0.5 cm. To study the grid size only, a suggested Ma_{LB} of no larger than 0.15 (He and Luo, 1997b) is used.

A sketch of the numerical model in this section is given in Fig. 5. The static open boundary wave generator with the AWA method is used to generate waves at the inlet open boundary, the AWA method is used to absorb waves at the outlet open boundary, and the periodic or slip boundary condition is applied to the side boundaries.

4.1. Spatial step

A proper grid size of the numerical model is evaluated through the differences in the wave profile and phase between the Boussinesq solitary wave theory (Svendsen, 2005) and the simulation results. From Fig. 6(a) to Fig. 6(d), an approach of the simulated wave profile to the theoretical wave profile with decreasing grid size or increasing wave height (H) in lattice units $H_{LB} = H/\delta_x$ could be observed. When the grid becomes finer than 1.0 cm ($H_{LB} > 8$), the simulated wave profiles show little change, which indicates a converged numerical result. The wave crest of the converged result is higher than the theoretical data indicate, and this difference could be interpreted according to the study of Wu and Hsiao (2018): the wave height of the solitary wave generated by the static open boundary wave generator will be higher than that according to wave theory. Therefore, the wave profiles at different times, instead of the theoretical wave profile, are chosen to calculate the dissipative error Δ_{cr},

$$\Delta_{cr} = \left(\eta_{\max,t_1} - \eta_{\max,t_2}\right)/H \tag{23}$$

Table 7
Pressure gauge positions.

No.	X (m)	Y (m)	Z (m)	No.	X (m)	Y (m)	Z (m)
1	10.85	0.20	0.18	2	10.85	0.12	0.26
3	10.85	0.04	0.10	4	10.89	0.04	0.30
5	11.05	0.12	0.30	6	10.97	0.20	0.30

where, $\eta_{\max,t_1}$ is the simulated wave crest elevation at $t = 4.0$ s and $\eta_{\max,t_2}$ is the simulated wave crest elevation at the last time $t = 16.0$ s. The dissipative error is shown in Fig. 6(e); it decreases from 1.15% to 0.59% as the grid size δ_x decreases from 4.0 cm to 0.7 cm, which is consistent with the announced discrepancy (0.68%) caused by the fluid viscosity (Chiang, 1992). When the grid size decreases to $\delta_x = 0.5$ cm, the dissipative error increases to 0.86%. When using a finer mesh, it is increasingly accurate to capture the dispersion and nonlinearity of the solitary wave, so the discrepancy decreases first. However, when the grid size is reduced to 0.5 cm, which is small enough to capture the dispersion and nonlinearity of the solitary wave, the numerical dissipation caused by too many grids in the horizontal direction becomes obvious. Fig. 6(e) indicates that grid sizes of $H_{LB} = 16$ and $H_{LB} = 24$ perform better than the other tested grid sizes.

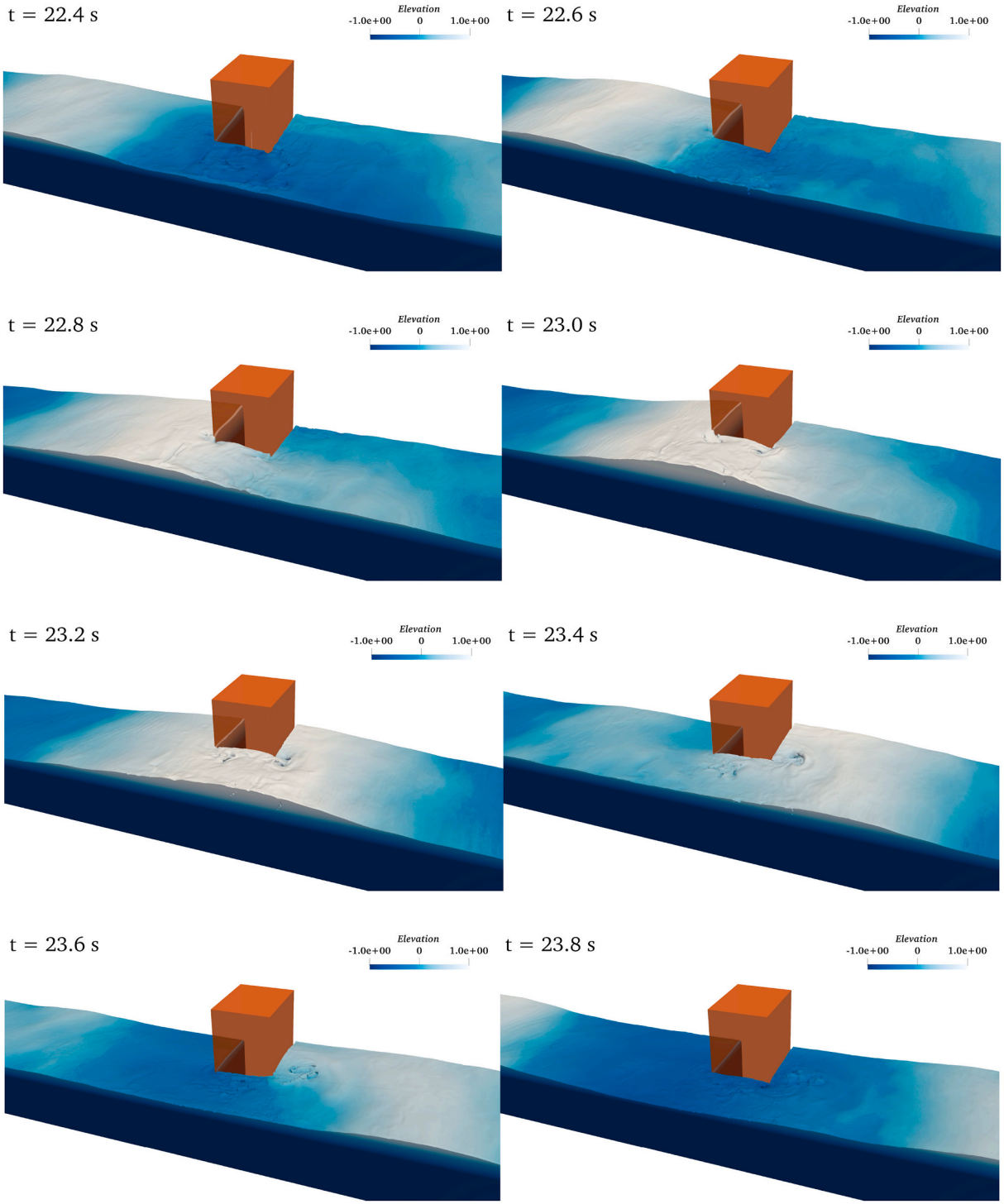

Fig. 9. Animation of the numerical simulations of the wave transformation on a vertical structure from 22.4 s to 23.8 s.

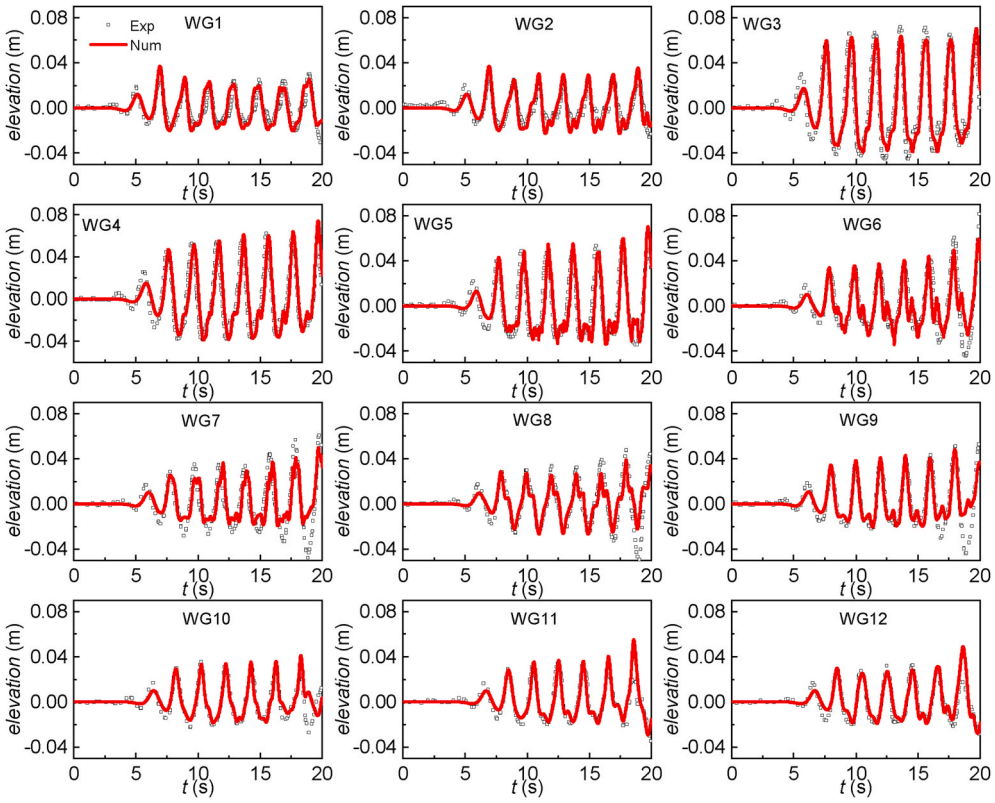

Fig. 10. Comparison of the numerical and experimental gauge elevations.

Table 8
The discrepancy in wave elevation between the numerical results and experimental data.

No.	Δ_{cr}(%)	Δ_{ph}(%)	No.	Δ_{cr}(%)	Δ_{ph}(%)
WG1	10.4	2.1	WG7	8.7	5.4
WG2	8.2	1.8	WG8	9.1	4.3
WG3	9.3	3.8	WG9	5.7	3.3
WG4	3.8	4.6	WG10	4.0	3.2
WG5	9.4	4.1	WG11	6.8	1.8
WG6	8.9	3.9	WG12	5.6	1.4

The discrepancy in the wave phase between the simulation result and the theoretical result is evaluated by $\Delta_{ph} = |x_{cr,s} - x_{cr,t}|/\lambda$, $x_{cr,s}$ is the simulated wave crest position at the end time, $x_{cr,t}$ is the theoretical wave crest position at the end time, and λ is the wavelength. The discrepancy in the wave phases is 1.15% for $H_{LB} = 4$ and reduces to 0.00% for $H_{LB} = 24$.

Overall, the simulated waves show good agreement with the wave theory for $H_{LB} = 16$, 24, with nearly no discrepancy in the wave phase and almost the same accuracy of $\Delta_{cr} \leq 1.0\%$. Hence, considering the computational costs, a grid size of $H_{LB} = 16$ can be finally recommended.

4.2. Temporal step

In the LB model, the determination of a proper time step closely relates to Mach number, which represents fluid compressibility. According to the definition of the Mach number, two values are given, namely the physical Mach number (Ma_{Phy}) and the LB Mach number (Ma_{LB}). The former is known and determined when the wave parameter is specified. Thus, the wave model will have the highest accuracy when Ma_{LB} is set equal to the Ma_{Phy}. However, the presented LB model is not established according to the Mach number similarity criterion. That is, the weak compressibility of the LB model is not consistent with real fluid motion, and the correlation between these two is unclear. Certainly, both overestimating and underestimating Ma_{LB} will cause a non-ignorable deviation of wave celerity from the real wave motion, causing hydrodynamic deviations to occur. For example, a strong correlation between Ma_{LB} and the pressure magnitude is observed (Ueberrueck and Janssen, 2017). As a result, a proper Ma_{LB} or proper time step needs to be determined to obtain satisfactory simulation results.

Simulations of different time steps corresponding to $Ma_{LB} = 0.128$, 0.096, 0.064, 0.032 and 0.016 are tested. Since the grid size determination test suggests $H_{LB} = 16$, the wave height in the lattice units is set to 16 in the time step determination tests. Fig. 7(a) shows the wave elevation of the case of $Ma_{LB} = 0.128$. The simulated wave crest is higher than and out of phase with the theoretical data. Fig. 7(b–d) shows the wave elevation for the smaller time steps of $Ma_{LB} = 0.064$, 0.032 and 0.016. The accuracy increases as the time step decreases, and the results for the time step of $Ma_{LB} = 0.064$ most closely agree with the theoretical results. Fig. 7(e) shows the discrepancy between the simulated wave and the theoretical wave. The discrepancy in wave crest increases from −0.71% to 1.30% as Ma_{LB} decreases from 0.128 to 0.016, which is caused by the cumulative numerical dissipation since the numerical iterations increase as Ma_{LB} decreases. The discrepancy in wave phases is 3.77% for $Ma_{LB} = 0.128$, reduces to 0.03% for $Ma_{LB} = 0.064$, and then increases to 1.28% for $Ma_{LB} = 0.016$. Overall, the simulated wave shows the best agreement with the wave theory for $Ma_{LB} = 0.064$, with an accuracy of $\Delta \leq 1.0\%$.

In summary, the grid sizes of $H_{LB} = 16$ and $Ma_{LB} = 0.064$ are the best choice for the present wave condition. Since the Ma_{LB} of the following cases is similar to the present solitary wave, the same Ma_{LB} is used in the following numerical tests and applications.

5. Application of numerical wave model and verification through experiments

In this section, the 3D LBM solver is used to simulate wave

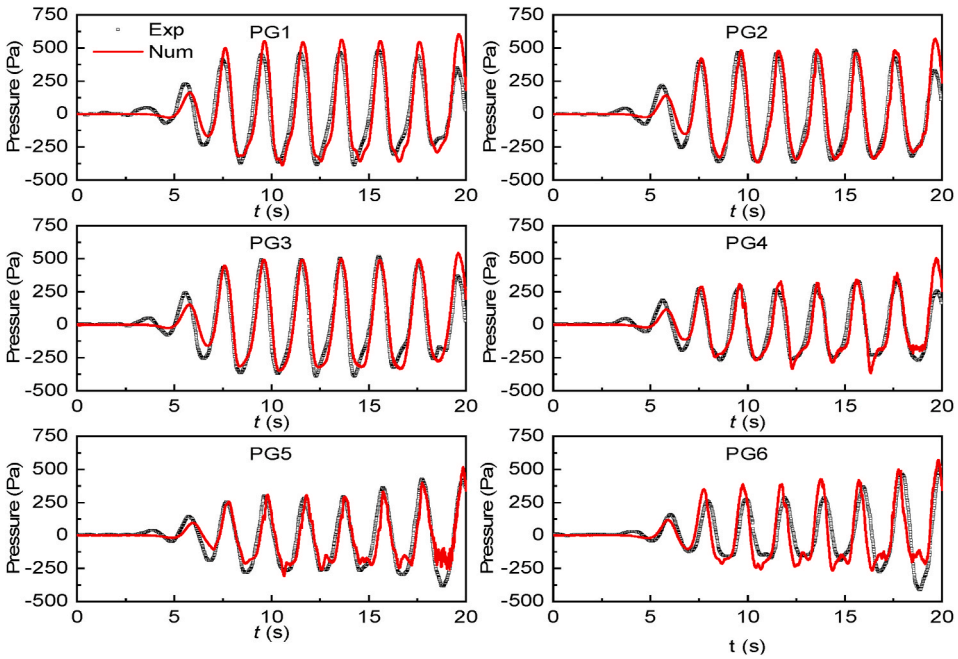

Fig. 11. Comparison of the numerical and experimental gauge pressures.

Table 9
The discrepancy in water pressure between the numerical results and experimental data.

No.	PG1	PG2	PG3	PG4	PG5	PG6
Δ_{cr}(%)	7.4	2.3	1.0	2.6	1.1	7.1

transformations at the laboratory scale. First, wave reflection and diffraction on a vertical structure in a narrow wave flume is simulated. Then, solitary wave propagation and breaking on a slope in a narrow wave flume is investigated. Finally, the numerical result of a solitary wave runup on a circular island in a large basin is presented. The details of the simulations carried out for this research are listed in Table 5, in which λ represents wavelength.

All the numerical cases are conducted on a Tianhe-1A supercomputer. Two Intel X5670 (2.9 GHz) CPUs are assembled for each computing node of the Tianhe-1A. The computational efficiency of simulation is described by the ratio (η_{sim}) of the simulation duration (t_{end}) to the simulation clock time (T_s) and the CPU cores (N_p) used for simulation, which is $\eta_{sim} = t_{end}/(T_s N_p)$.

5.1. Wave reflection and diffraction on a vertical structure

Vertical structures, such as vertical breakwaters, are commonly used in coastal engineering. The use of numerical models to accurately simulate the reflection and diffraction of waves around vertical structures, especially fully 3D wave reflections, is important for studying the response of vertical structures under waves. To test the accuracy of the 3D LBM solver on the simulation of the full 3D reflection and diffraction of waves on the structure, a complex reflection and diffraction of a cnoidal wave on a vertical structure is simulated and compared with a physical experiment.

5.1.1. Description of the physical experiments

The physical experiments (Lara et al., 2012) were conducted in the wave tank of a University of Cantabria laboratory. The tank is 22 m long, 58.5 cm wide, 78 cm high and equipped with a piston-type wave maker. Fig. 8 shows a sketch of the physical experiment, where the X and Z directions are horizontal and the Y direction is vertical. A vertical structure 24 cm long, 30 cm wide and 70 cm high was placed at a distance of 11.28 m from the mean position of the wave maker.

In the experiment, the water elevation was measured with a frequency of 360 Hz at 12 positions. The arrangement of the wave gauges is shown in Fig. 8, and the coordinates of the wave gauges are listed in Table 6. The distribution of the wave gauges was asymmetrical, 4 gauges

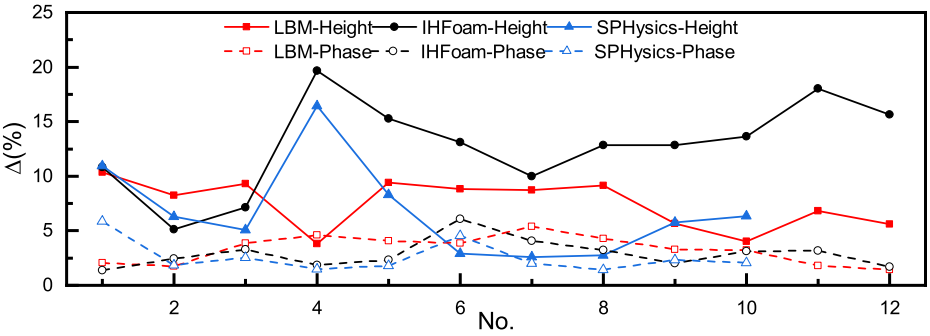

Fig. 12. Mean discrepancies in wave crest and phase between the numerical results simulated by the presented solver, IHFoam and SPHysics and the experimental data among the 12 wave gauges. Solid lines represent the discrepancies in the wave crest, and dashed lines represent the discrepancies in the wave phase.

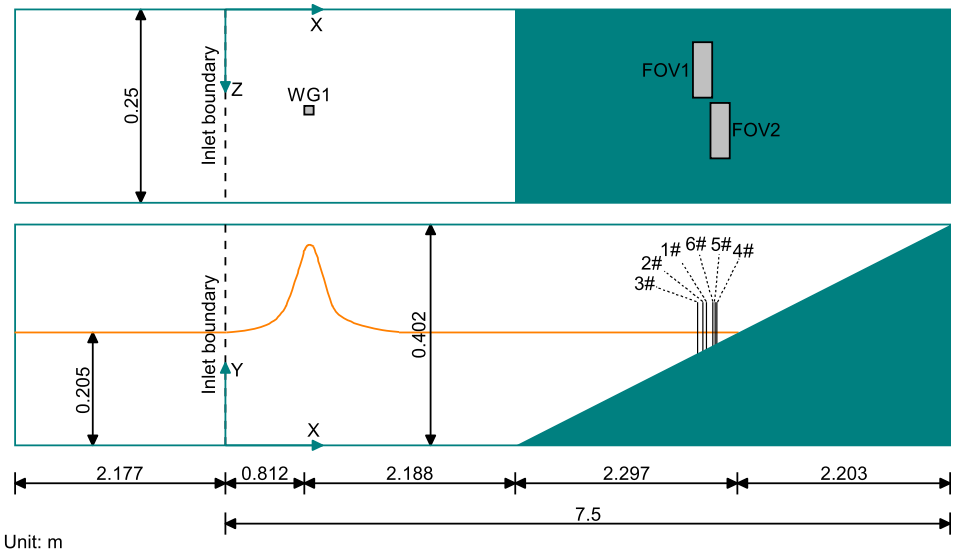

Fig. 13. Sketch of the numerical experimental setup of solitary wave breaking on a sloping beach.

Table 10
Velocity gauge positions of the wave breaking experiment.

	Gauge 1	Gauge 2	Gauge 3	Gauge 4	Gauge 5	Gauge 6
x (m)	4.977	4.937	4.887	5.085	5.065	5.041

were placed in front of the structure, and 8 gauges were placed behind the structure. Among them, wave gauges 1 and 3 were used to study the wave reflection, and wave gauges 5, 6, 7 and 9 were used to study the wave diffraction. The wave pressure was measured on the surface of the impervious structure at six positions, and the coordinates of the pressure gauges are listed in Table 7.

Ten different wave conditions were tested in the experiment. The wave height of the solitary wave ranges from 0.05 m to 0.14 m, and the water depth changes from 0.25 m to 0.45 m. The wave height of the

Table 11
Mean velocity (mm/s) of the fluid in FOV1 and FOV2 at different times.

	t^*	U_m	t^*	U_m	t^*	U_m	t^*	U_m
Exp. Data	31.35	641	31.63	753	31.77	791	32.18	510
Simulation results		654		756		797		511

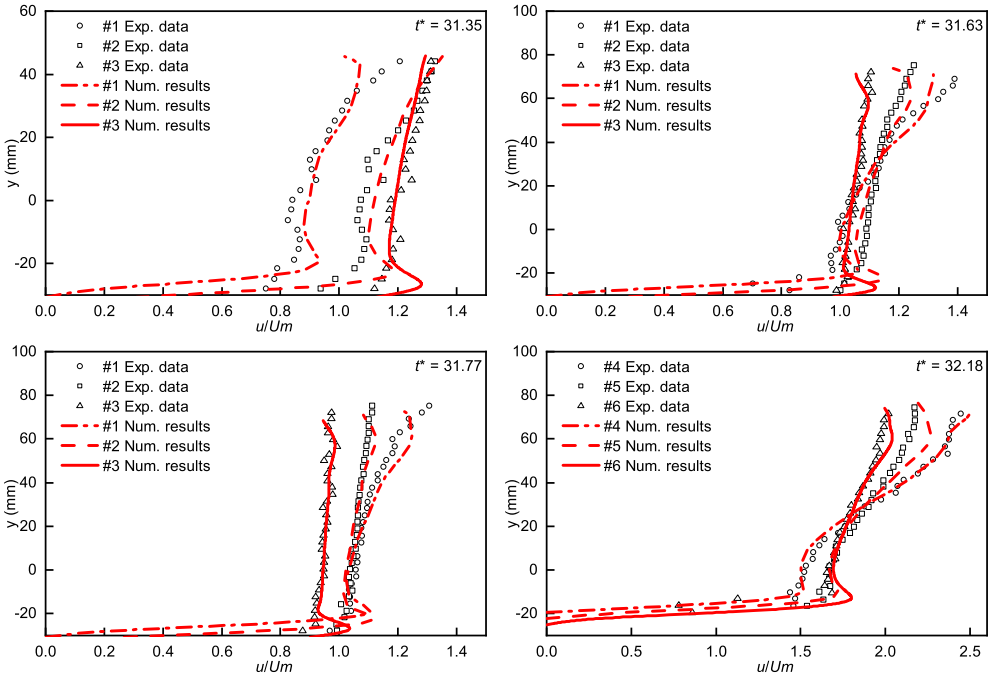

Fig. 14. Comparison of the vertical profiles of horizontal velocity between the simulation and experimental results at the 6 velocity gauges.

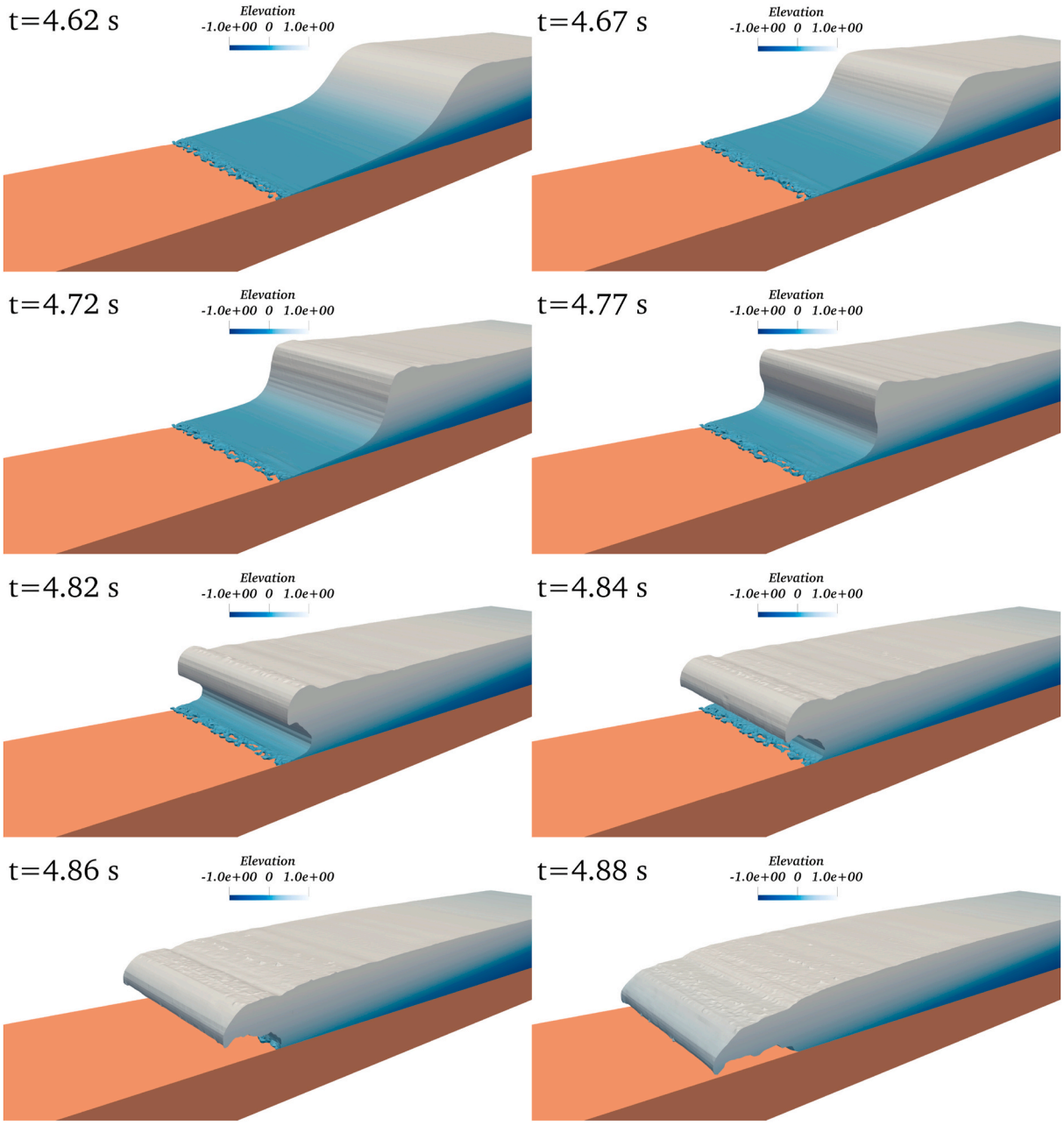

Fig. 15. Animation of simulated wave surfaces from t = 4.62 s–4.88 s.

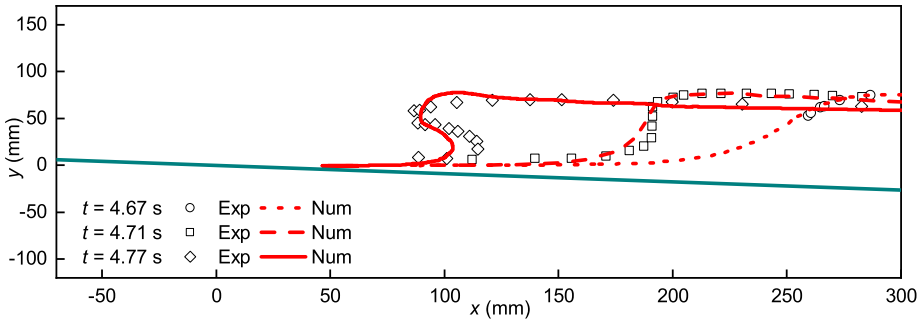

Fig. 16. Solitary wave surfaces of the experiment and numerical simulation during the breaking process from 4.67 s to 4.77 s. Symbols represent the surface in the experiment, and lines represent the surface in the numerical simulation.

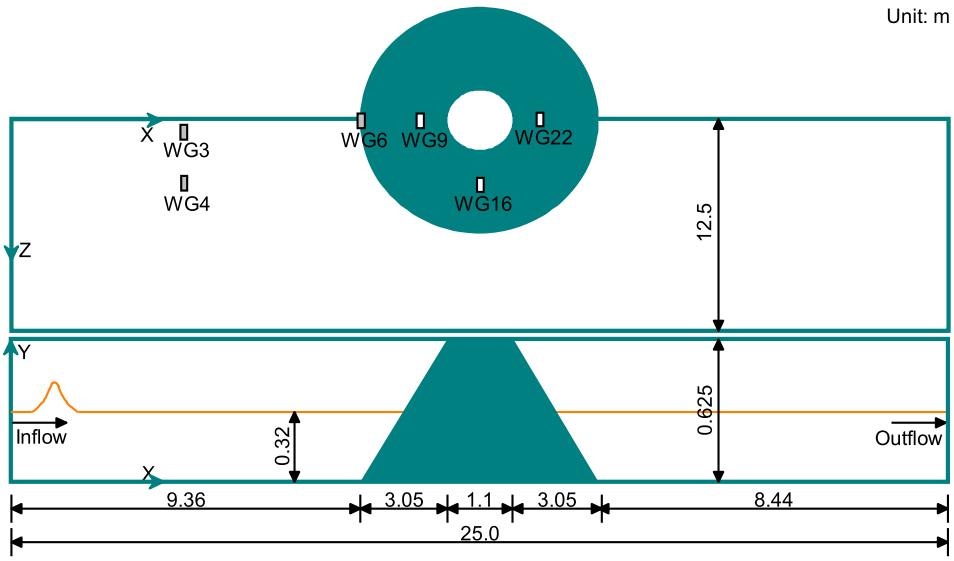

Fig. 17. Sketch of the numerical experimental setup of solitary wave runup on a circular island.

Table 12
Wave gauges positions of the wave runup experiment.

No.	X (m)	Z (m)	No.	X (m)	Z (m)
3	7.56	0.75	4	7.56	2.25
6	9.36	0.00	9	10.36	0.00
16	12.96	2.58	22	15.56	0.00

regular wave is 0.06 m, the period is 2.0 s, and the water depth is 0.25 m.

5.1.2. Simulation results

The numerical flume has a length (L) of 20.17 m, a width (W) of 0.585 m and a height (H) of 0.38 m, and the inlet boundary is 0.43 m from the mean position of the wave maker. The regular wave condition is selected for numerical simulation. The wave condition and numerical model parameters are given in Table 5, and the wave period is $T = 2.0$ s. The surface of the vertical structure and the outflow boundary are treated with a nonslip boundary condition; a slip boundary condition is adopted on both sides of the wave tank. During the numerical simulation, the water elevation at the positions where the 12 wave gauges are located is calculated, the coordinates of the wave gauges are listed in Table 6, and the sampling frequency is 200 Hz. Following the physical experiment, the outlet boundary is replaced by a solid wall. The simulated water elevation and pressure are compared with the experimental data measured at the 12 wave gauges and 6 pressure gauges respectively. The performance and accuracy of the presented model in the description of wave reflection and diffraction is discussed in the following subsection.

Fig. 9 shows the temporal variation in the simulated wave transformation around the vertical structure. From $t = 22.4$ s to $t = 23.0$ s, the wave crest in front of the vertical structure is higher than that of the incident wave due to partial reflection. Motions from $t = 23.0$ s to $t = 23.8$ s represent a wave diffraction process lasting $0.5T$, during which time several vortices form at the corners of the vertical structure, along with waves propagating to the back of the structure. The combined action of reflection and diffraction creates a complex water surface in space and time.

Fig. 10 shows the comparison of the simulated water elevations at the 12 wave gauge locations with those of the experimental data (Lara et al., 2012). Both the simulated wave crest and wave phase agree well with the experimental data. The mean discrepancy, which is calculated by averaging the discrepancy in the first five normal waves, between the numerical results and experimental data are listed in Table 8. The discrepancy in the wave crest is calculated as $\Delta_{cr} = |\eta_{\max,s} - \eta_{\max,m}|/H$, $\eta_{\max,s}$ is the simulated wave crest elevation, and $\eta_{\max,m}$ is the experimental wave crest elevation. The discrepancy in the wave phase is calculated as $\Delta_{ph} = |t_{cr,s} - t_{cr,m}|/T$, $t_{cr,s}$ is the simulated wave crest time, and $t_{cr,m}$ is the experimental wave crest time. The mean discrepancy in the 12 wave gauges in the wave crest is 7.5%, and the mean discrepancy in the wave phase is 3.3%, which indicates good performance of the presented model in the simulation of wave reflection and diffraction.

The simulated wave crests in gauge 1 and gauge 3 are slightly lower than that of the experiment, which indicates a smaller reflected wave energy of the simulation. The simulated wave crests at gauge 5, gauge 6 and gauge 9 are slightly higher than the experimental wave crests, which indicates a slightly larger diffraction. Since the shape of the reflected waves depends on the size and surface roughness of the vertical structure used in the experiment and the nonslip boundary condition used on the surface of the vertical structure in the numerical model cannot completely reflect the roughness effect of the structure surface, differences between the simulation results and experimental data may be inevitable.

The hydrodynamic pressure generated by waves gradually increases upward and achieves a maximum close to the still water level. Wave-induced dynamic pressure is positively correlated with wave amplitude. Among the 6 pressure gauges, gauge 1 and gauge 6 are at the same height, gauge 2 and gauge 5 are at the same height, and gauge 3 and gauge 4 are at the same height. Comparing the above three pairs, the pressures at gauges 4, 5, and 6 located between the structure and the lateral boundary are smaller than values at gauges 1, 2, and 3 in front of the structure. Fig. 11 shows the comparison of simulated water pressures at 6 pressure gauge locations with the experimental data. Both the pressure crest and the pressure phase agree well with that of the experimental data. The mean discrepancies between the simulated pressure and experimental data are listed in Table 9. The discrepancy in the pressure crest is calculated as $\Delta_{cr} = |p_{\max,s} - p_{\max,m}|/1250$, where $p_{\max,s}$ is the simulated pressure crest and $p_{\max,m}$ is the experimental pressure crest. The mean discrepancy is calculated by averaging the discrepancy in the first six normal waves. The mean discrepancy among the six pressure gauges in the crest is 3.6%. Quite good agreement with the experimental results is achieved at gauges 2, 3, 4 and 5. Wave crests that are slightly higher than those of the experiment are observed at gauge 1 and gauge 6. The high simulated pressure at gauge 6 corresponds to a high wave crest, and both are caused by a slightly larger

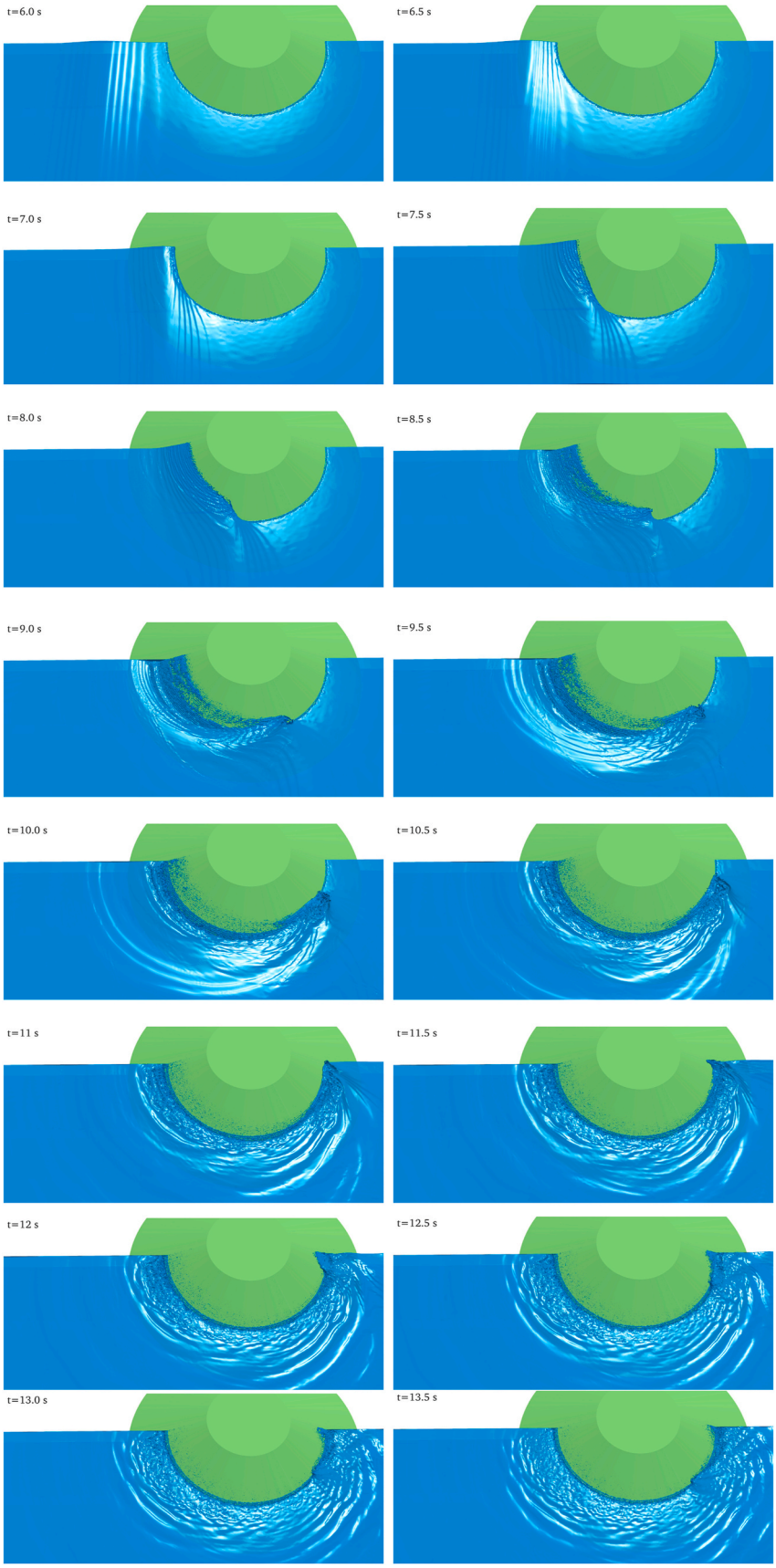

Fig. 18. Animation of the wave runup process by numerical simulation from 6 s to 13.5 s.

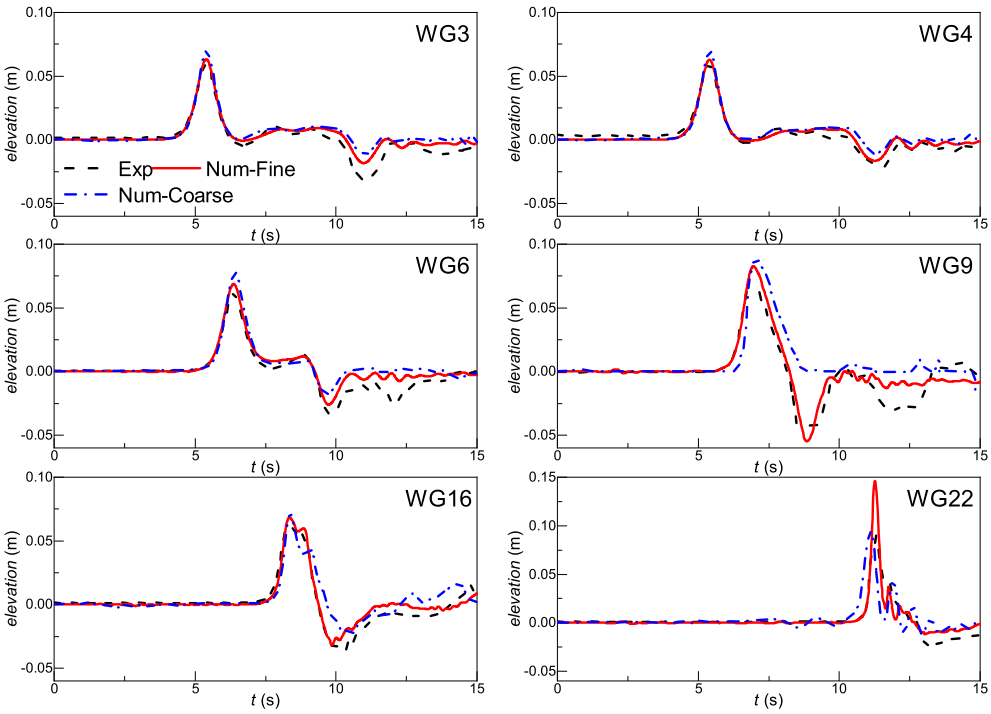

Fig. 19. Comparison of the elevations at six wave gauges between the simulation results and experimental data. The red solid line represents the numerical results using a fine mesh, and the blue dashed line represents the numerical results using a coarse mesh. The black dashed line represents the experimental data. (For interpretation of the references to colour in this figure legend, the reader is referred to the Web version of this article.)

Table 13
The discrepancies in wave crest between the numerical results and experimental data.

No.	WG3	WG4	WG6	WG9	WG16	WG22
Δ_{cr}(%)	5.6	4.5	12.6	30.7	9.3	86.1

diffraction. In general, good performance of the 3D LBM solver in terms of pressure simulation is demonstrated in this work.

5.1.3. Comparison of different solvers

The accuracy of the presented 3D LBM solver is compared with those of two other popular solvers by comparison of their discrepancies in wave crest and phase (Fig. 12). The other two solvers considered are IHFoam (Lara et al., 2012) and SPHysics (Wen et al., 2016). As shown in Fig. 12, the average discrepancies in wave crest for the presented solver, IHFoam and SPHysics are 7.5%, 12.8% and 6.7%, respectively. The average discrepancies in the wave phase for the above three solvers are 3.3%, 2.9% and 2.6%, respectively. The presented LBM solver shows a similar accuracy to SPHysics in terms of the wave profile and phase and a slightly higher accuracy than IHFoam in terms of the wave profile. In general, the presented solver is approximately as accurate as IHFoam and SPHysics.

In summary, the presented 3D LBM solver can accurately simulate the combined action of wave reflection and diffraction with the same accuracy as the IHFoam solver and the SPHysics solver.

5.2. Solitary wave breaking on a slope

Wave breaking is of great significance for nearshore sediment transport and coastal protection. The breaking process is a complex 3D flow (Biausser et al., 2004). Many detailed measurements of solitary wave breaking on sloping beaches have been carried out (Alagan Chella et al., 2017; Huang and Hwang, 2015; Pringle et al., 2016; Swigler, 2009). Here, an experiment of solitary wave breaking on a slope is used to demonstrate the accuracy of the present VOF model in simulating wave breaking.

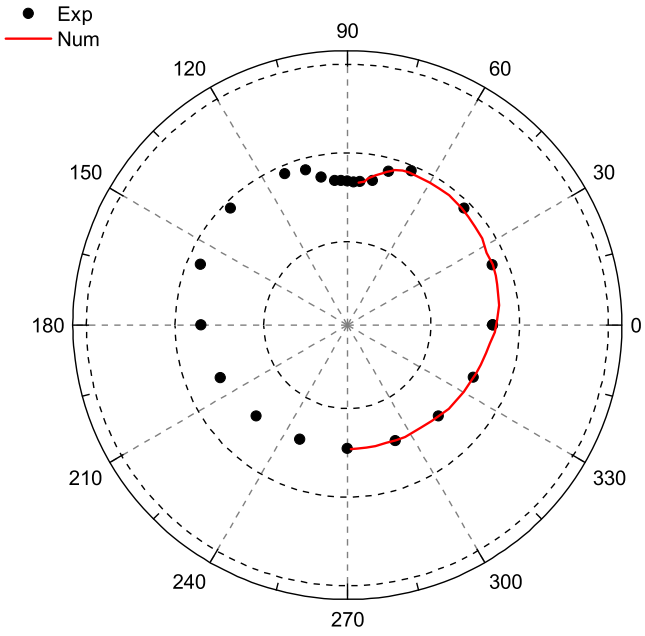

Fig. 20. Comparison of wave runup height on the circular island between the simulation results and experimental data. The red solid line represents the simulation results, and the black circles represent the experimental data. (For interpretation of the references to colour in this figure legend, the reader is referred to the Web version of this article.)

5.2.1. Description of the physical experiments

The physical experiment was conducted in the wave tank of the

Table 14
Hardware configurations on one board.

Platform	Processor	Memory	Total cores	Interconnection speed (Gbps)
Tianhe-1A	2 × Intel X5670@2.93 GHz	6 × DDR3-1333-4 GB	12	40
Tianhe-3 prototype	Phytium FT2000+/32@2.2 GHz	4 × DDR4-2666-4 GB	32	200

Table 15
Computational efficiency $\eta_{sim} = T_s/(T_{wall}N_p)$ of the 3D LBM, the IHFoam and the SPHysics solvers in the simulation of wave propagation in a wave flume.

Model	N_G (M.)	T_s (s)	N_p (cores)	f_{core} (GHz)	T_{wall} (hr)	η_{sim} ($hr^{-1}core^{-1}s \times 10^{-3}$)
3D LBM solver	77.2	24	120	2.6	14.3	14.0
	10.6	24	120	2.6	1.0	200.0
IHFoam solver	1.5	20	64	2.6	72.0	4.3
SPHysics solver	2.1	15	64	2.8	96.0	2.4

Hydrodynamic Laboratory at the University of the Oslo (Mo et al., 2013); this wave tank is 25 m long, 0.5 m wide and 1 m high, using a piston-type wave maker. In the experiment, the mean water depth (h) is maintained at 0.205 m, the vertical direction is the Y-axis, and the horizontal direction X_{phy} starts from the shoreline. A sloping beach is placed 5.177 m from the mean position of the wave maker, with an inclination of 5.1°.

In the experiment, a wave gauge was placed at the position of $x_{phy} =$ 4.485 m, and the measuring frequency was 1000 Hz. Particle image velocimetry (PIV) was used to measure the flow of two fields of view (FOVs) near the shoreline, with the first FOV at 260 mm $< x_{phy} <$ 460 mm and the second FOV closer to the shoreline at 80 mm $< x_{phy} <$ 280 mm. The measurement frequency was 1000 Hz. A high-speed camera was also used in the experiment to record the wave breaking process.

In the experiment, the wave height of the solitary wave was 6.8 cm, and the wave broke on the beach as a plunge wave breaker.

5.2.2. Simulation results

Fig. 13 shows a sketch of this numerical model of this experiment. The positive X-axis of the numerical model is the negative X-axis of the physical experiment, the origin is set at the inlet boundary, and the distance from the beach to the inlet boundary is shortened to 3.0 m. The numerical model has a length of 7.5 m, a width of 0.25 m and a height of 0.40 m. The parameters of the numerical model are given in Table 5. The bottom of the tank and the surface of the beach have a nonslip boundary condition, and a slip boundary condition is adopted on both sides of the tank. During the numerical simulation, the wave surface and the vertical profile of the flow velocity at six positions are calculated. The positions of the gauges are given in Table 10, and the measuring frequency is 100 Hz.

The simulated horizontal velocities are compared with the experimental results. The mean velocities simulated in FOV1 and FOV2 are consistent with the experimental data, as shown in Table 11, in which the time is normalized as $t^* = t\sqrt{g/h}$. The vertical profiles of the horizontal velocity normalized by the mean velocity at the 6 wave gauges also agree well with the measurements (Fig. 14). The four plots in Fig. 14 show that the velocity near the interface exceeds the bottom velocity. This phenomenon is consistent with wave transformation characteristics: as a wave climbs a slope, the wave front will steepen due to the upper fluid speeding up and bottom fluid slowing down.

In Fig. 15, the wave crest becomes steeper and nearly breaks during the 0.15 s from $t = 4.62$ s to $t = 4.77$ s. As the upper fluid continues moving, the wave steepness becomes too high to sustain a continuous wave surface and then breaks. This phenomenon is described by the simulation in the period from $t = 4.82$ s to $t = 4.88$ s. The simulated wave profiles at different times are compared with the measured data, as displayed in Fig. 16. The simulation results are generally consistent with the experimental data, with a few differences, such as the relatively smaller nappe in front of the simulated wave crest, when a large surface deformation and rapid change in the fluid field occur during wave breaking, because the presented VOF model cannot exactly describe the surface of the plunging wave and an insufficient number of grid cells are used to describe the wave.

Generally, the 3D LBM solver can reasonably simulate wave transformation and breaking on a beach, and the regularity of the variation in the simulated flow field, such as the breaking form and the breaking location, agrees well with that observed experimentally.

5.3. Runup on a circular island

In recent years, Indian and Pacific Ocean tsunamis have occurred frequently, and people in tsunami-affected areas have been greatly affected. The runup of tsunamis in nearshore regions will cause serious damage to lives and property, so the study of tsunami protection and mitigation has become a research hotspot in recent years. Accurate simulation of the hydrodynamic response around structures under tsunami can provide effective protection schemes. Therefore, the 3D LBM solver is applied to simulate runup experiments of solitary waves on circular islands to test the capability of the model to simulate the

Table 16
Best computational performance obtained on the Tianhe-3 prototype.

Model	N_G (M.)	Np (cores)	T_{wall} (hr)	η_{sim} ($hr^{-1}core^{-1}s \times 10^{-3}$)
3D LBM solver	46.4	4800	0.32	9.8
IHFoam solver	8.0	2048	0.85	8.6

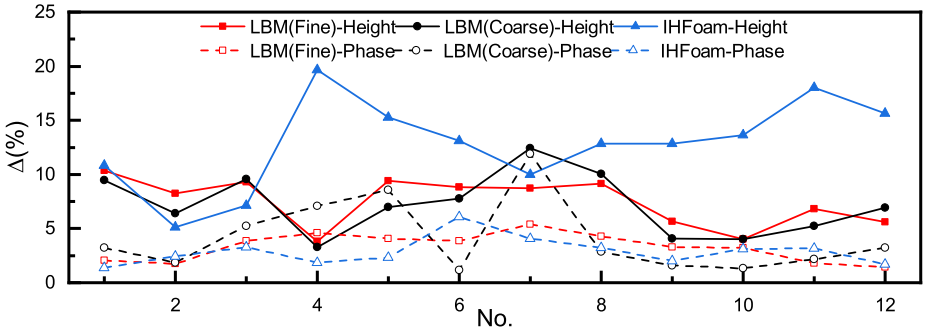

Fig. 21. Mean discrepancies in the wave crest and phase among the numerical results simulated by the presented LBM solver, IHFoam and experimental data at the 12 wave gauges. Solid lines represent the discrepancy in the wave crest, and dashed lines represent the discrepancy in the wave phase.

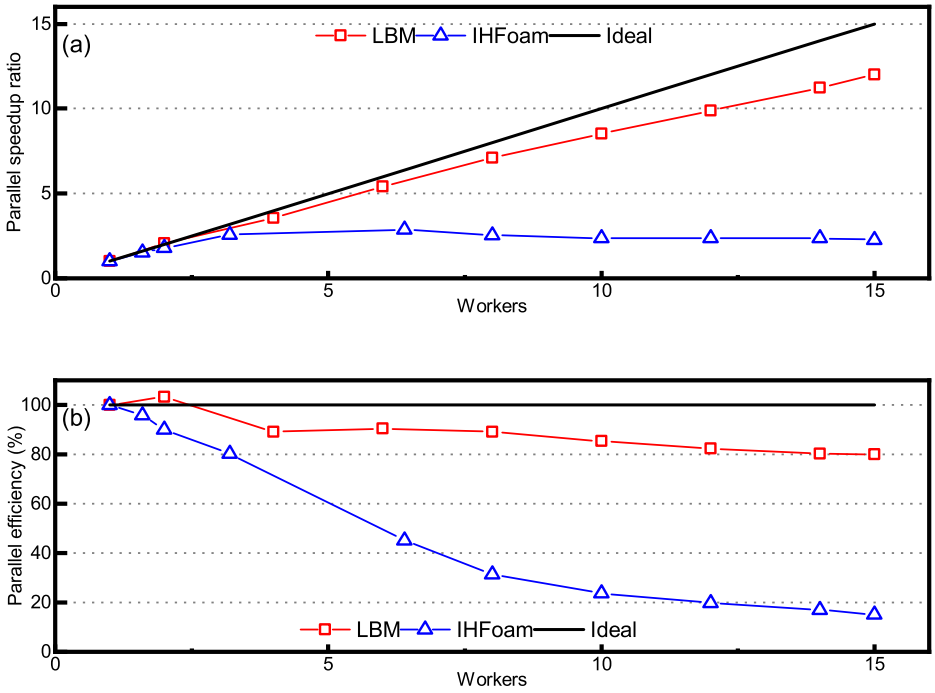

Fig. 22. Parallel speedup ratio and efficiency of the presented LBM solver and IHFoam solver in wave basin cases on the Tianhe-3 prototype. In the figures, one worker corresponds to 320 CPU cores.

combined action of wave shoaling, refraction, diffraction, reflection and breaking on a beach during a tsunami.

5.3.1. *Description of the physical experiments*

The physical experiments (Briggs et al., 1995; Liu et al., 1995) were conducted in the wave basin of the U.S. Army Engineering Waterways Laboratory Station, Coastal Engineering Research Center. This basin was 25 m long, 30 m wide and equipped with a directional spectral wave generator (DSWG), which was composed of four modules of 15 paddles. Fig. 17 shows a sketch of the physical model. The horizontal direction included the X-axis and Z-axis, the origin of the X-axis was at the plane where the DSWG was located, and the origin of the Z-axis was at the plane where the central axis of the circular island was located. The island was in the center (12.96 m, 0 m, 0 m) of the basin and had a top surface diameter of 2.2 m, bottom surface diameter of 7.2 m, slope gradient of 1:4, and height of 0.625 m. Six groups (three wave heights of 0.05 m, 0.064 m and 0.20 m, two water depths of 0.32 m and 0.42 m) of solitary waves were tested in the physical wave flume.

In the experiment, 27 wave gauges with a measuring frequency of 25 Hz were placed. Among them, only measurement data of six gauges (gauges 3, 4, 6, 9, 16 and 22) are disclosed in the corresponding paper (Briggs et al., 1995; Liu et al., 1995). The arrangement of the six wave gauges is shown in Fig. 17, and their locations are given in Table 12. The first two gauges (gauge 3 and gauge 4) are arranged parallel to the DSWG to measure the incident wave height.

In the experiment, 20 sets of runup gauges were arranged to measure the maximum runup on the island. The gauges were arranged on the island at an interval of a 22.5°, except where a denser arrangement was used on the right side of the backside of the island to measure the wave runup more accurately.

5.3.2. *Simulation results*

The data measured in the physical experiments show good symmetry about the Z-axis. To reduce the computational cost, only the right half of the physical experimental basin is simulated. The numerical domain is 25 m long and 12.5 m wide. The wave condition $H/h = 0.2$ is selected to perform the simulation. Slip boundary conditions are applied to the bottom of the tank, nonslip boundary conditions are applied to the island surface, and slip boundary conditions are applied to both sides of the tank.

In the numerical simulation, the water elevation at six wave gauges and the maximum wave runup on the island are calculated, and the sampling frequency of the water elevation is 100 Hz. The maximum wave runup is calculated at 50 locations with a spacing of 3.6° along a circular line of investigation and filtered with the surface elevation during simulation.

To evaluate the performance of the presented 3D LBM solver in the simulation of wave runup, the simulated water elevation and maximum runup are compared with the measured data, and the transformation process is presented.

Fig. 18 shows the process of wave transformation on the circular island in the simulation. From 6.0 s to 8.5 s, wave runup occurs at the front of the island. The solitary wave climbs onto the highest position at the front of the island and breaks there; while in the relatively deep water, the wave continues to propagate, and wave refraction forms. From 9.0 s to 13.5 s, a combined wave action of diffraction and reflection occurs. Under this combined action, the wave crest line transforms into a fish scale type. After propagating around the island, the solitary wave finally breaks at the backside of the island.

Fig. 19 shows a comparison of the simulated water elevations using two grid sizes (1 cm and 1.6 cm) with the experimental data at the six same locations (Briggs et al., 1995). Compared with the results obtained by the simulation with a coarse mesh, the gauge elevations obtained by using the simulation with a fine mesh are closer to the experimental measurement data. The main difference between the two meshes is the accuracy of the characterization of the circular island surface. The fine mesh can better capture the shape of the island and improve the accuracy of the first reflected wave in the simulation so that the solver can more accurately calculate the intensity and phase of the reflected wave after the solitary wave encounters the island. The mean discrepancy between the results of the simulated wave using a fine mesh and the experimental data are listed in Table 13. The discrepancy in the wave crest is calculated as $\Delta_{cr} = |\eta_{\max,s} - \eta_{\max,m}|/H$, where $\eta_{\max,s}$ is the simulated wave crest elevation and $\eta_{\max,m}$ is the experimental wave crest

elevation. The simulated elevations at gauges 9 and 22 are slightly higher than the experimental data, and such a difference was also reported by Higuera et al. (2013b). The discrepancies in wave height and phase mainly result from the different surface frictions of the island between the experiment and the simulation.

Fig. 20 shows the comparison of the simulated wave runup with the experimental data. Although the simulated reflection wave height is slightly different than that of the experiment, as shown in Fig. 19, the simulated wave runup is consistent with the experimental data.

In summary, the presented 3D LBM solver can accurately simulate the process of wave runup on a circular island with reasonable accuracy.

6. Discussion on the performance of parallel computation

In this section, the performance of the presented solver with parallel computation is discussed in detail. First, the computational performance and accuracy of the presented solver is discussed by in comparison with those of two other solvers for wave propagation simulation in wave flumes. Then, the parallel scalability of the presented LBM solver on the Tianhe-3 prototype, when used to simulate wave propagation in wave basins, is compared with the IHFoam solver in OpenFOAM.

The computing platform used in the first part of this study is Tianhe-1A, and that in the second part is the Tianhe-3 prototype. Table 14 gives the hardware configuration of Tianhe-1A and the Tianhe-3 prototype.

6.1. Wave flume case

A wave flume is generally used for performing unidirectional wave propagation experiments at large scales. The water depth used in experiments is relatively deep and the width of flumes is relatively narrow, mostly 1–2 m, compared to other physical experiments. Under such experimental conditions, the number of grids used in the corresponding numerical model is related to the length of the flume, and when dividing subdomains for parallel computation, the model will be equally divided along the length of the flume, and the amount of data synchronization between adjacent subdomains is small. The flume experiment in section 5.1 is used as the benchmark to compare the performance of IHFoam, SPHysics and the solver presented in this paper.

Table 15 shows the computational efficiency of the three solvers when simulating the experiment discussed in section 5.1. The Tianhe-1A platform is used for numerical simulation with the presented LBM solver. The processor used by the Tianhe-1A platform is similar to those used by Lara et al. (2012) and Wen et al. (2016). The computational efficiency of the presented LBM solver in this experiment is 14.0×10^{-3} $\mathrm{hr}^{-1}\mathrm{core}^{-1}\mathrm{s}$. Compared with the efficiency of IHFoam (Lara et al., 2012), which is 4.3×10^{-3} $\mathrm{hr}^{-1}\mathrm{core}^{-1}\mathrm{s}$, and that of SPHysics (Wen et al., 2016), which is 2.4×10^{-3} $\mathrm{hr}^{-1}\mathrm{core}^{-1}\mathrm{s}$, the presented LBM solver is 3.3 and 5.8 times faster, respectively.

The vertical grid size used for the LBM solver is half of that used for IHFoam. In addition, due to the advantages of unstructured grids and polyhedral elements, IHFoam can use a horizontal grid size of 1–4 cm, thereby greatly reducing the number of girds. To match the number of grids used by IHFoam as close as possible, we performed another simulation using a grid size of 0.75 cm. Fig. 21 shows the comparison of the mean discrepancy between the two grids using the presented LBM solver and IHFoam. The mean accuracy of the simulation results obtained by the presented LBM solver (7.2% in wave crest) is still better than that of IHFoam (12.8% in wave crest), even if the grid size is doubled. However, the computational efficiency of the presented LBM solver with the coarse mesh is 200.0×10^{-3} $\mathrm{hr}^{-1}\mathrm{core}^{-1}\mathrm{s}$, which is 46.5 times that of the IHFoam solver.

The above results show that the presented LBM solver has the same accuracy as the IHFoam and SPHysics solvers based on NSE. The computational efficiency of the presented LBM solver is much higher than that of the IHFoam and SPHysics solvers, and the highest efficiency of the LBM solver can reach 46 times that of the IHFoam solver.

6.2. Wave basin case

Wave basins are generally used to solve 3D problems such as wave propagation, transformation, and wave-structure interactions. The vertical size of the simulation domain is often much smaller than the horizontal size, and the grid size is mainly controlled by the wave height and the size of the structure, resulting in a very large number of grids compared to that for a wave flume. When dividing subdomains for parallel computation, the simulation domain will be divided into $N \times M$ equal-sized regions in the horizontal direction, and the amount of data synchronization between adjacent subdomains will be considerable. A large number of computing resources need to be allocated centrally to simulate wave transformation in the wave basin. Under this computing resource organization structure, the LBM has great advantages in applications due to its high parallel scalability. In the following, the physical model experiment in section 5.3 is used as a benchmark to compare the parallel computational efficiency of IHFoam and the solver developed in this paper on the supercomputing platform.

Table 16 shows the computational efficiency obtained by the two solvers using the 128–4800 CPU cores on the Tianhe-3 prototype to solve the problem of solitary wave runup on a circular island. The IHFoam solver is based on OpenFOAM-v1906. The IHFoam solver obtains the highest computational efficiency when using 2048 CPU cores, and the shortest wall clock time is 0.85 h. The computational efficiency obtained by the presented LBM solver has a good positive correlation with the number of CPU cores used (Fig. 22). The minimum wall clock time when using 4800 CPU cores is 0.32 h. Fig. 22 shows the parallel speedup ratio and efficiency of the two solvers as the number of workers (one worker represents 320 CPU cores) increases. The LBM solver has a very good parallel scalability, and the parallel efficiency can attain 80% even when using 4800 CPU cores. For IHFoam, the parallel speedup ratio first increases and then decreases slowly. When the number of CPU cores exceeds 2048, the speedup ratio starts to decrease, and the parallel efficiency decreases to 17% when using 4800 CPU cores.

The results of the wave basin case indicate that the 3D LBM solver developed in this paper has good parallel scalability and computational efficiency on the supercomputing platform. The parallel efficiency of the 3D LBM solver is more than 4 times that of a solver such as IHFoam based on the RANS-VOF model. In this section, although the number of grids used by the LBM solver is five times that used by the IHFoam solver, the best computational efficiency obtained by the 3D LBM solver is still higher than that of the IHFoam solver.

In general, the simulation results obtained in this section clearly prove that on the supercomputing platform, the LBM solver developed in this paper has a much higher parallel efficiency and parallel scalability than the IHFoam solver.

7. Conclusions

In this study, we proposed a new collision operator, and built a 3D LBM numerical wave solver with high computational efficiency and parallel scalability based on this operator. The solver uses LBM for NS-VOF model to simulate surface waves, and the static open boundary condition is implemented for wave generation and absorption. The optimal parameters for the presented model are determined by comparison with the theoretical solution.

The new D3Q27 MRT collision operator proposed in this study is more stable than the five commonly-used collision operators. In wave simulations, the proposed collision operator enables good performance of the 3D numerical wave solver even when the local Ma_{LB} reaches 0.14.

The LBM for NS-VOF model is successfully applied to describe wave reflection, diffraction, shoaling and breaking during wave-structure interaction. A comparison of the simulation results with the experimental data shows that the present model developed in this paper performs well in most wave transformation phenomena except in solitary wave breaking when runup occurs on a slope, and this is due to the

insufficient accuracy of the VOF model.

The presented 3D LBM solver shows higher computational efficiency than IHFoam and SPHysics solvers when used to simulate wave transformation in both wave flumes and basins. In addition, on the supercomputing platform, the presented 3D LBM solver also exhibits a much higher parallel speedup ratio and parallel efficiency than the IHFoam solver.

In the future, a water-air two-phase LB-ICM model (Dinesh Kumar et al., 2019) is expected to better describe the wave breaking problem. In addition, local mesh refinement (Lagrava et al., 2012) could be introduced to significantly reduce the amount of computation required for a certain engineering problem and thus increase the spatial scale that can be simulated by the 3D LBM solver.

CRediT author statement

Guangwei Liu: Conceptualization, Methodology, Software, Validation, Formal analysis, Investigation, Writing – original draft. **Jinfeng Zhang**: Conceptualization, Writing – review & editing, Resources. **Qinghe Zhang**: Conceptualization, Writing – review & editing, Supervision, Project administration.

Declaration of competing interest

The authors declare that they have no known competing financial interests or personal relationships that could have appeared to influence the work reported in this paper.

Acknowledgments

This work was supported by the National Natural Science Foundation of China (Grant Nos. U1906231 and 51979190), the Natural Science Foundation of Tianjin (Grant No. 19JCZDJC40200) and Guangdong Water Conservancy Science and Technology Innovation Project (Grant No. 2017-17). The first author would like to thank Lin Xie at the Tianjin Research Institute for Water Transport Engineering for the valuable discussions. The work was carried out at the National Supercomputer Center at Tianjin, and the calculations were performed on Tianhe-1A and Tianhe-3 prototype. This paper benefited from helpful comments and suggestions from the referees and the editor.

References

Aggarwal, A., Bihs, H., Myrhaug, D., Chella, M.A., 2019. Characteristics of breaking irregular wave forces on a monopile. Appl. Ocean Res. 90, 101846. https://doi.org/10.1016/j.apor.2019.06.003.

Akbari, H., Namin, M.M., 2013. Moving particle method for modeling wave interaction with porous structures. Coast. Eng. 74, 59–73. https://doi.org/10.1016/j.coastaleng.2012.12.002.

Alagan Chella, M., Bihs, H., Myrhaug, D., Muskulus, M., 2017. Breaking solitary waves and breaking wave forces on a vertically mounted slender cylinder over an impermeable sloping seabed. J. Ocean Eng. Mar. Energy 3 (1), 1–19. https://doi.org/10.1007/s40722-016-0055-5.

Badarch, A., Fenton John, D., Hosoyamada, T., 2020. Application of free-surface immersed-boundary lattice Boltzmann method to waves acting on coastal structures. J. Hydraul. Eng. 146 (2), 04019062 https://doi.org/10.1061/(ASCE)HY.1943-7900.0001679.

Biausser, B., Grilli, S.T., Fraunie, P., Marcer, R., 2004. Numerical analysis of the internal kinematics and dynamics of 3-D breaking waves on slopes. Int. J. Offshore Polar 14 (4), 247–256.

Bihs, H., Kamath, A., Alagan Chella, M., Aggarwal, A., Arntsen, Ø.A., 2016. A new level set numerical wave tank with improved density interpolation for complex wave hydrodynamics. Comput. Fluids 140, 191–208. https://doi.org/10.1016/j.compfluid.2016.09.012.

Bogner, S., Ammer, R., Rüde, U., 2015. Boundary conditions for free interfaces with the lattice Boltzmann method. J. Comput. Phys. 297, 1–12. https://doi.org/10.1016/j.jcp.2015.04.055.

Briggs, M.J., Synolakis, C.E., Harkins, G.S., Green, D.R., 1995. Laboratory experiments of tsunami runup on a circular island. Pure Appl. Geophys. 144 (3), 569–593. https://doi.org/10.1007/BF00874384.

Carrica, P.M., Wilson, R.V., Stern, F., 2007. An unsteady single-phase level set method for viscous free surface flows. Int. J. Numer. Methods Fluid. 53 (2), 229–256. https://doi.org/10.1002/fld.1279.

Chiang, C.M., 1992. The Applied Dynamics of Ocean Surface Waves Advanced Series on Ocean Engineering, vol. 1. World Scientific, p. 768. https://doi.org/10.1142/0752.

Culpo, M., 2010. Current Bottlenecks in the Scalability of OpenFOAM on Massively Parallel Clusters, Partnership for Advanced Computing in Europe, Bruxelles, Belgium. https://doi.org/10.5281/zenodo.807482.

d'Humières, D., Ginzburg, I., Krafczyk, M., Lallemand, P., Luo, L.-S., 2002. Multiple-relaxation-time lattice Boltzmann models in three dimensions. Phil. Trans. R. Soc. A 360, 437–451. https://doi.org/10.1098/rsta.2001.0955.

Dalrymple, R.A., Rogers, B.D., 2006. Numerical modeling of water waves with the SPH model. Coast. Eng. 53, 141–147. https://doi.org/10.1016/j.coastaleng.2005.10.004.

Dinesh Kumar, E., Sannasiraj, S.A., Sundar, V., 2019. Phase field lattice Boltzmann model for air-water two phase flows. Phys. Fluids 31 (7), 072103. https://doi.org/10.1063/1.5100215.

Fakhari, A., Bolster, D., Luo, L.-S., 2017. A weighted multiple-relaxation-time lattice Boltzmann method for multiphase flows and its application to partial coalescence cascades. J. Comput. Phys. 341, 22–43. https://doi.org/10.1016/j.jcp.2017.03.062.

Garcia, N., Lara, J.L., Losada, I.J., 2004. 2-D numerical analysis of near-field flow at low-crested permeable breakwaters. Coast. Eng. 51 (10), 991–1020. https://doi.org/10.1016/j.coastaleng.2004.07.017.

Guo, X., Rogers, B.D., Lind, S., Stansby, P.K., 2018. New massively parallel scheme for Incompressible Smoothed Particle Hydrodynamics (ISPH) for highly nonlinear and distorted flow. Comput. Phys. Commun. 233, 16–28. https://doi.org/10.1016/j.cpc.2018.06.006.

Guo, Z., Chu-Guang, Z., Bao-Chang, S., 2002. An extrapolation method for boundary conditions in lattice Boltzmann method. Phys. Fluids 14 (6), 2007–2010. https://doi.org/10.1063/1.1471914.

He, F., Zhang, H., Huang, C., Liu, M., 2020. Numerical investigation of the solitary wave breaking over a slope by using the finite particle method. Coast. Eng. 156, 103617. https://doi.org/10.1016/j.coastaleng.2019.103617.

He, X., Luo, L.-S., 1997a. Lattice Boltzmann model for the incompressible Navier–Stokes equation. J. Stat. Phys. 88 (3–4), 927–944. https://doi.org/10.1023/B:JOSS.0000015179.12689.e4.

He, X., Luo, L., 1997b. Theory of the lattice Boltzmann method: from the Botlzmann equation to the lattice Boltzmann equation. Phys. Rev. E 56 (6), 6811–6817. https://doi.org/10.1103/PhysRevE.56.6811.

Higuera, P., Lara, J.L., Losada, I.J., 2013a. Realistic wave generation and active wave absorption for Navier–Stokes models: application to OpenFOAM®. Coast. Eng. 71, 102–118. https://doi.org/10.1016/j.coastaleng.2012.07.002.

Higuera, P., Lara, J.L., Losada, I.J., 2013b. Simulating coastal engineering processes with OpenFOAM®. Coast. Eng. 71, 119–134. https://doi.org/10.1016/j.coastaleng.2012.06.002.

Huang, Z.-C., Hwang, K.-S., 2015. Measurements of surface thermal structure, kinematics, and turbulence of a large-scale solitary breaking wave using infrared imaging techniques. Coast. Eng. 96, 132–147. https://doi.org/10.1016/j.coastaleng.2014.12.005.

Janssen, C., Krafczyk, M., 2010. A lattice Boltzmann approach for free-surface-flow simulations on non-uniform block-structured grids. Comput. Math. Appl. 59 (7), 2215–2235. https://doi.org/10.1016/j.camwa.2009.08.064.

Janssen, C.F., Grilli, S.T., Krafczyk, M., 2013. On enhanced non-linear free surface flow simulations with a hybrid LBM–VOF model. Comput. Math. Appl. 65 (2), 211–229. https://doi.org/10.1016/j.camwa.2012.05.012.

Kang, S.K., Hassan, Y.A., 2013. The effect of lattice models within the lattice Boltzmann method in the simulation of wall-bounded turbulent flows. J. Comput. Phys. 232 (1), 100–117. https://doi.org/10.1016/j.jcp.2012.07.023.

Körner, C., Thies, M., Hofmann, T., Thürey, N., Rüde, U., 2005. Lattice Boltzmann model for free surface flow for modeling foaming. J. Stat. Phys. 121 (1–2), 179–196. https://doi.org/10.1007/s10955-005-8879-8.

Krafczyk, M., Tolke, J., Luo, L.-S., 2003. Large eddy simulation with a multiple-relaxation-time LBE model. Int. J. Mod. Phys. B 17 (1), 33–39. https://doi.org/10.1142/S0217979203017059.

Krüger, T., et al., 2017. The lattice Boltzmann method - principles and practice. In: Graduate Texts in Physics. Springer Nature, Switzerland. https://doi.org/10.1007/978-3-319-44649-3.

Kumar, E.D., Sannasiraj, S.A., Sundar, V., 2019. Lattice Boltzmann simulation of free surface flow impact on a structure. Phys. Rev. E 99, 023308. https://doi.org/10.1103/physreve.99.023308.

Lagrava, D., Malaspinas, O., Latt, J., Chopard, B., 2012. Advances in multi-domain lattice Boltzmann grid refinement. J. Comput. Phys. 231 (14), 4808–4822. https://doi.org/10.1016/j.jcp.2012.03.015.

Lara, J.L., del Jesus, M., Losada, I.J., 2012. Three-dimensional interaction of waves and porous coastal structures: Part II: experimental validation. Coast. Eng. 64, 26–46. https://doi.org/10.1016/j.coastaleng.2012.01.009.

Lenz, S., et al., 2019. Towards real-time simulation of turbulent air flow over a resolved urban canopy using the cumulant lattice Boltzmann method on a GPGPU. J. Wind Eng. Ind. Aerod. 189, 151–162. https://doi.org/10.1016/j.jweia.2019.03.012.

Lin, P., Liu, P.L.F., 1999. Internal wave-maker for Navier-Stokes equations models. J. Waterw. Port, Coast. Ocean Eng. 125 (4), 207–215. https://doi.org/10.1061/(ASCE)0733-950X(1999)125:4(207).

Liu, G.-w., Zhang, Q.-h., Zhang, J.-f., 2020. Development of two-dimensional numerical wave tank based on lattice Boltzmann method. J. Hydrodyn. 32 (1), 116–125. https://doi.org/10.1007/s42241-019-0039-8.

Liu, G., Zhang, Q., Zhang, J., 2019. Numerical wave simulation using a modified lattice Boltzmann scheme. Comput. Fluids 184, 153–164. https://doi.org/10.1016/j.compfluid.2019.03.005.

Liu, P.L.-F., Cho, Y.-S., Briggs, M.J., Kanoglu, U., Synolakis, C.E., 1995. Runup of solitary waves on a circular island. J. Fluid Mech. 302, 259–285. https://doi.org/10.1017/S0022112095004095.

Liu, P.L.F., Lin, P., Chang, K.-A., Sakakiyama, T., 1999. Numerical modeling of wave interaction with porous structures. J. Waterw. Port, Coast. Ocean Eng. 125 (6), 322–330. https://doi.org/10.1061/(ASCE)0733-950X(1999)125:6(322).

Liu, X., Lin, P., Shao, S., 2015. ISPH wave simulation by using an internal wave maker. Coast. Eng. 95, 160–170. https://doi.org/10.1016/j.coastaleng.2014.10.007.

Luo, L.-S., Liao, W., Chen, X., Peng, Y., Zhang, W., 2011. Numerics of the lattice Boltzmann method: effects of collision models on the lattice Boltzmann simulations. Phys. Rev. E 83 (5), 056710. https://doi.org/10.1103/PhysRevE.83.056710.

Maza, M., Lara, J.L., Losada, I.J., 2015. Tsunami wave interaction with mangrove forests: a 3-D numerical approach. Coast. Eng. 98, 33–54. https://doi.org/10.1016/j.coastaleng.2015.01.002.

Maza, M., Lara, J.L., Losada, I.J., 2016. Solitary wave attenuation by vegetation patches. Adv. Water Resour. 98, 159–172. https://doi.org/10.1016/j.advwatres.2016.10.021.

Miliani, S., Montessori, A., Rocca, M.L., Prestininzi, P., 2021. Dam break modelling: the LBM as the way towards fully 3D, large scale applications. J. Hydraul. Eng. https://doi.org/10.1061/(ASCE)HY.1943-7900.0001879. In press.

Mo, W., Jensen, A., Liu, P.L.-F., 2013. Plunging solitary wave and its interation with a slender cylinder on a sloping beach. Ocean Eng. 74, 48–60. https://doi.org/10.1016/j.oceaneng.2013.09.011.

Morrison, H.E., Leder, A., 2018. Sediment transport in turbulent flows with the lattice Boltzmann method. Comput. Fluids 172, 340–351. https://doi.org/10.1016/j.compfluid.2018.04.015.

Peng, C., Geneva, N., Guo, Z., Wang, L.-P., 2018. Direct numerical simulation of turbulent pipe flow using the lattice Boltzmann method. J. Comput. Phys. 357, 16–42. https://doi.org/10.1016/j.jcp.2017.11.040.

Pringle, W.J., Yoneyama, N., Mori, N., 2016. Two-way coupled long wave - RANS model: solitary wave transformation and breaking on a plane beach. Coast. Eng. 114, 99–118. https://doi.org/10.1016/j.coastaleng.2016.04.011.

Ren, B., Wen, H., Dong, P., Wang, Y., 2014. Numerical simulation of wave interaction with porous structures using an improved smoothed particle hydrodynamic method. Coast. Eng. 88, 88–100. https://doi.org/10.1016/j.coastaleng.2014.02.006.

Safi, M.A., 2016. Efficient Computations for Multiphase Flow Problems Using Coupled Lattice Boltzmann-Level Set Methods. Technischen Universität Dortmund, Dortmund, Germany, p. 155.

Sato, K., Koshimura, S., 2020. Validation of the MRT-LBM for three-dimensional free-surface flows: an investigation of the weak compressibility in dam-break benchmarks. Coast Eng. J. 62 (1), 53–68. https://doi.org/10.1080/21664250.2019.1672124.

Schäffer Hemming, A., Klopman, G., 2000. Review of multidirectional active wave absorption methods. J. Waterw. Port, Coast. Ocean Eng. 126 (2), 88–97. https://doi.org/10.1061/(ASCE)0733-950X(2000)126:2(88).

Schornbaum, F., Rude, U., 2015. Massively parallel algorithm for the lattice Boltzmann method on non-uniform grids. SIAM J. Sci. Comput. 38 (2), 96–126. https://doi.org/10.1137/15M1035240.

Shao, S., et al., 2006. Simulation of wave overtopping by an incompressible SPH model. Coast. Eng. 53 (9), 723–735. https://doi.org/10.1016/j.coastaleng.2006.02.005.

Sitompul, Y.P., Aoki, T., 2019. A filtered cumulant lattice Boltzmann method for violent two-phase flows. J. Comput. Phys. 390, 93–120. https://doi.org/10.1016/j.jcp.2019.04.019.

Suga, K., Kuwata, Y., Takashima, K., Chikasue, R., 2015. A D3Q27 multiple-relaxation-time lattice Boltzmann method for turbulent flows. Comput. Math. Appl. 69 (6), 518–529. https://doi.org/10.1016/j.camwa.2015.01.010.

Svendsen, I.A., 2005. Introduction to nearshore hydrodynamics. In: Advanced Series on Ocean Engineering, 24. World Scientific, Singapore, p. 744. https://doi.org/10.1142/5740.

Swigler, D.T., 2009. Laboratory Study Investigating the Three-Dimensional Turbulence and Kinematic Properties Associated with a Breaking Solitary Wave. Master Thesis. Texas A&M University, College Station, USA, p. 162.

Thorimbert, Y., Latt, J., Cappietti, L., Chopard, B., 2016. Virtual wave flume and Oscillating Water Column modeled by lattice Boltzmann method and comparison with experimental data. Int. J. Mar. Energy 14, 41–51. https://doi.org/10.1016/j.ijome.2016.04.001.

Thuerey, N., 2003. A Lattice Boltzmann Method for Single-phase Free Surface Flows in 3D. Master Thesis. University of Erlangen-Nuremberg, Erlangen-Nuremberg, Germany, p. 60.

Ueberrueck, M., Janssen, C.F., 2017. On the applicability of lattice Boltzmann single-phase models for the simulation of wave impact in LNG tanks. Int. J. Offshore Polar 27 (4), 390–396. https://doi.org/10.17736/ijope.2017.jc679.

Wen, H., Ren, B., Dong, P., Wang, Y., 2016. A SPH numerical wave basin for modeling wave-structure interactions. Appl. Ocean Res. 59, 366–377. https://doi.org/10.1016/j.apor.2016.06.012.

Williams, S., Carter, J., Oliker, L., Shalf, J., Yelick, K., 2009. Optimization of a lattice Boltzmann computation on state-of-the-art multicore platforms. J. Parallel Distr. Comput. 69 (9), 762–777. https://doi.org/10.1016/j.jpdc.2009.04.002.

Wu, Y.-T., Hsiao, S.-C., 2018. Generation of stable and accurate solitary waves in a viscous numerical wave tank. Ocean Eng. 167, 102–113. https://doi.org/10.1016/j.oceaneng.2018.08.043.

Yong, W.-A., Zhao, W., Luo, L.-S., 2016. Theory of the Lattice Boltzmann method: derivation of macroscopic equations via the Maxwell iteration. Phys. Rev. E 93 (3), 033310. https://doi.org/10.1103/PhysRevE.93.033310.